BSc THESIS – CHEMICAL SCIENCE & ENGINEERING

SOLVENT ANNEALING AS A POST-TREATMENT: TOWARDS SINGLE CRYSTALLINE EPITAXIAL $MAPbI_3$

Author: RILDA SOJATI

Committee member: PROF. DR. J.G.E GARDENIERS
Head supervisor: PROF. M. MORALES MASIS
Daily supervisor: IR. J.S.S. SOLOMON SATHIARAJ

Date: July 17, 2023

INORGANIC MATERIALS SCIENCE (IMS)
FACULTY OF SCIENCE AND TECHNOLOGY

UNIVERSITY OF TWENTE.

ABSTRACT

The demand for clean and sustainable energy has driven extensive research in the field of photovoltaics to develop high-efficiency solar cells with low-cost fabrication processes. Perovskite materials, such as $MAPbI_3$, have shown remarkable efficiency progress in the last decade due to their excellent optoelectronic properties. However, they are primarily used in their polycrystalline form characterized by small grain sizes, boundaries and defects. To further enhance the optoelectronic properties of perovskites, it is crucial to increase the grain size, ultimately progressing towards a single-crystalline structure.

This thesis focuses on solvent annealing (SA) as a post-treatment method to increase the grain size of epitaxial $MAPbI_3$ thin films. SA involves annealing the thin films while introducing a polar-aprotic solvent vapour, specifically DMSO in this case. Parameters such as the SA time, solvent quantity, and temperature are investigated to assess their impact on the structure, morphology, and optical properties of the epitaxial thin films. Experimental characterization techniques including XRD, AFM, and PL are employed to evaluate the effects.

The obtained results highlight the effectiveness of SA in promoting grain growth in $MAPbI_3$ thin films, although the preservation of epitaxy remains a challenge. Furthermore, the presence of excess PbI_2 precursor and low perovskite phase conversion are evident in most results. These issues are attributed to prolonged exposure of the thin films to DMSO vapour, leading to thermal degradation of the perovskite over time. Following this, a new SA method (SA method 2) was introduced to address these challenges, resulting in improved outcomes. This method showcased a significant improvement, with a grain size increase from 32.5 to 75 nm. Although this grain size increase is small, it further attests to the efficacy of the SA treatment and highlights the promising potential for further optimization of the SA parameters. Further investigation and optimization of the SA treatment are therefore crucial, as they hold promise for advancing the development of high-quality epitaxial $MAPbI_3$ perovskite thin films, particularly for application in solar cells.

CONTENTS

LIST OF ABBREVIATIONS AND SYMBOLS

AFM	Atomic Force Microscopy
ASA	After Solvent Annealing
ATA	After Thermal Annealing
BSA	Before Solvent Annealing
BTA	Before Thermal Annealing
DMF	Dimethylformamide
DMSO	Dimethyl Sulfoxide
FWHM	Full Width Half Maximum
MA	Methylammonium
MAI	Methylammonium Iodide
PL	Photoluminescence spectroscopy
PLD	Pulsed Laser Deposition
PV	Photovoltaic
SA	Solvent Annealing
UHV	Ultra-high Vacuum
XRD	X-Ray Diffraction

c	Speed of light in vacuum
Eg	Band gap
h	Planck's constant
J	Joules
K	Kelvin
λ	Wavelength
μm	Micrometer
nm	Nanometer
pm	Picometer
eV	Electron volt

1. INTRODUCTION

The increasing demand for clean and sustainable energy has driven extensive research in the field of photovoltaics (PV) over the past decade, positioning it as a renewable, emission-free and flexible energy source [1-2]. Solar cells play a vital role by utilizing the PV technology to convert sunlight directly into electricity. Researchers are actively involved in the development of high-efficiency solar cells with low-cost fabrication processes to meet the growing demand for sustainable energy [2]. Figure 1 shows the efficiency of the top performing solar cell technologies from 1976 to present. It is evident from the figure that emerging PV technologies have made remarkable progress in terms of efficiency, now comparable to the conventional silicon solar cells. Notably, perovskite materials have shown rapid improvements, achieving an impressive efficiency of 26% [3-4].

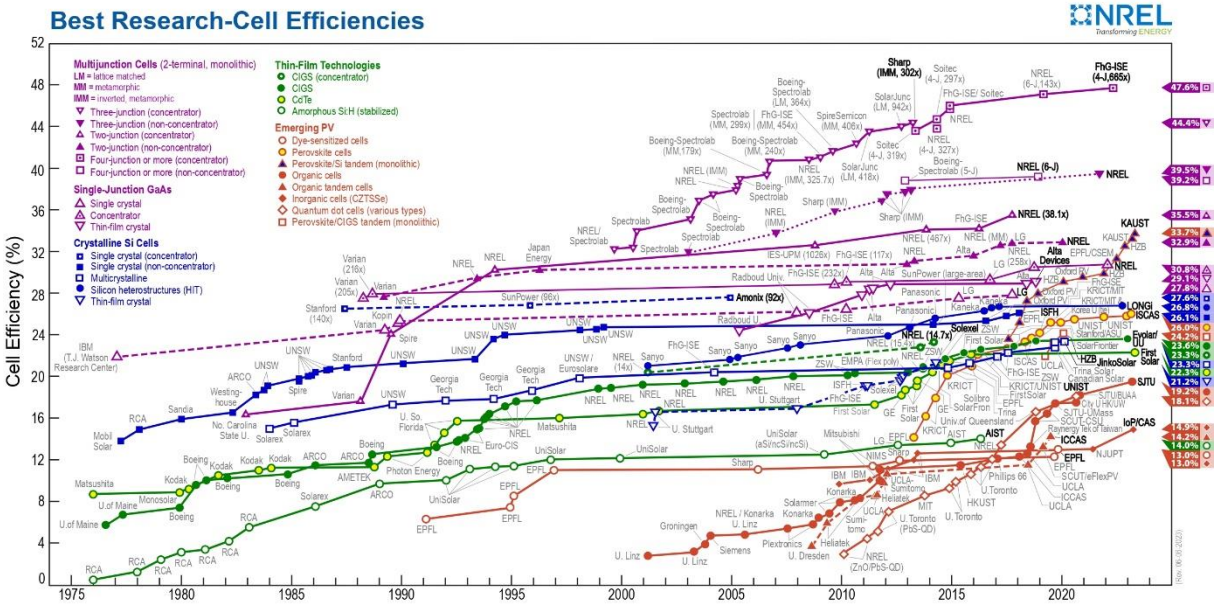

Figure 1: The development of the highest confirmed research-based solar cells efficiencies throughout the years of 1976 to 2023. The conventional Si cells are shown in blue and the emerging PV devices are shown in red, with perovskite cells shown in ● symbol. [4]

Inorganic-organic lead halide perovskite materials have demonstrated excellent optoelectronic properties such as high optical absorption coefficient, tuneable bandgaps, long-range carrier diffusion and high carrier mobility [3,5]. They are commonly used as the absorber layer of the solar cell, where they absorb the most light (photons) and give rise to electrons and holes needed to produce the current [6]. The chemical formula of the halide perovskite is ABX_3, where A is a monovalent cation, B is a divalent cation and X is a halide. Methylammonium lead triiodide, $MAPbI_3$, where A is methylammonium (MA), B is lead (Pb) and X is iodine (I), is one of the most widely used and best-performing halide perovskite materials due to its good optoelectronic properties and stability [7-9]. Figure 2 shows the perovskite structure of $MAPbI_3$.

To date, halide perovskite materials are mostly used in their polycrystalline form due to the uncontrollable nucleation of the deposited material, leading to small grain sizes with grain boundaries and other surface defects [10]. These grain boundaries and defects result in a high density of surface traps that can act as recombination centres, impairing the mobility of charge carriers and reducing the overall performance of the solar cells. One way to address this issue is by improving the morphology of the halide perovskite layer. Compared to polycrystalline films, single-crystalline halide perovskites have no internal grain boundaries or defects, low charge trap density, higher stability (incl. thermal stability) and better optoelectronic properties

overall [11]. For example, $MAPbI_3$ single crystals have roughly two orders of magnitude of higher carrier mobility and carrier diffusion length than polycrystalline thin films [12]. However, achieving a single-crystalline structure in halide perovskite materials is often very challenging due to its complexity and the methods required. Therefore, a lot of research goes into finding methods to increase the grain size, with the goal of achieving a single-crystalline structure.

Various fabrication techniques have been employed to increase the grain size of halide perovskite films. These methods, which can be applied either as a pre-treatment or as a post-treatment, include additive engineering [9, 13-15], interface engineering [16-17], solvent engineering [18-19], gas-assisted flow [20-22] and solvent annealing [23-26]. These techniques, like additive engineering and interface engineering, have proven effective in increasing grain size but often involve complex processes and require precise control. In contrast, solvent annealing (SA) offers a simple and scalable approach that is highly effective in promoting grain growth, e.g., SA-induced grain growth is usually substantially greater than thermal annealing-induced or using additive engineering [27]. This post-treatment technique involves annealing the halide perovskite thin films while introducing a polar-aprotic solvent vapour such as dimethylformamide (DMF) or dimethyl sulfoxide (DMSO) [24].

The Optoelectronic materials research of the IMS department of the University of Twente [28] has already successfully grown epitaxial thin films of $MAPbI_3$ via pulsed laser deposition (PLD). Epitaxial films are at an advantage over polycrystalline films, due to having a single crystal orientation rather than random grain orientations. However, despite this, the epitaxial thin films still exhibit small grain sizes with grain boundaries (illustrated in Figure 4). Moving from polycrystalline to epitaxial $MAPbI_3$ films with large grain sizes is a promising route for manufacturing high-quality and scalable perovskite products to bring them to the industry while studying fundamental material properties [29]. This thesis aims to use the solvent annealing treatment to increase the grain size of the epitaxial $MAPbI_3$ thin films, with the ambitious goal of achieving a single-crystalline epitaxial $MAPbI_3$ structure. Therefore, the main research question driving this investigation is as follows:

"What are the optimal parameters of the solvent annealing treatment to increase the grain size of epitaxial $MAPbI_3$ thin films and how does it affect the structure and optical properties?"

2. THEORETICAL BACKGROUND

This section dives into the theoretical background of the $MAPbI_3$ halide perovskite, providing essential information on its crystal structure and phases. Additionally, the significance of grain size and boundaries, optoelectronic properties, epitaxial growth, solvent annealing, and the characterization techniques used are detailed. These insights lay the groundwork for a comprehensive understanding of $MAPbI_3$ and set the stage for the subsequent experimental investigations.

2.1 Crystal structure and phases of $MAPbI_3$

$MAPbI_3$ follows the perovskite crystal structure denoted by ABX_3. The A-site is occupied by methylammonium cation (MA^+), the B-site by lead cation (Pb^{2+}) and the X-site by iodine anion (I^-). The Pb^{2+} and I^- coordinate in an octahedral shape, while the MA^+ and I^- bond through weak hydrogen bonding. Figure 2 shows the crystal structure of a perovskite, which consists of corner-sharing BX_6 octahedra that form a 3D network. The A^+ cations reside in the B – X framework cuboctahedra spaces.

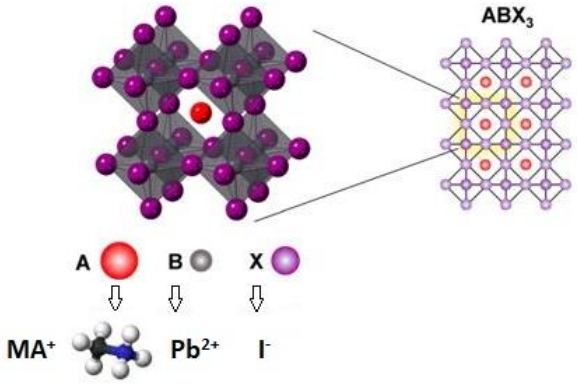

Figure 2: Crystal structure of perovskite and $MAPbI_3$. The ionic radii of MA+, Pb2+ and I- are 2.17, 1.19 and 2.20 Å respectively [30]. Adopted from [31].

The crystal structure, and hence properties, of the $MAPbI_3$ changes due to various external factors, such as temperature. $MAPbI_3$ has been reported to undergo three different structural phases: orthorhombic, tetragonal, and cubic [32]. The order-disorder of MA^+ cations plays a role in phase transitions [33]. Figure 3 shows the three different phases of $MAPbI_3$ together, along with the chemical bonds between I and H atoms.

The orthorhombic phase is found at low temperatures (below 160K) with the *Pnma* space group and is characterized by a fully ordered arrangement of MA^+ cations in the crystal structure. The tetragonal phase is usually stable at room temperature and found between 160 to 330K with the *14/mcm* space group. In this phase, the MA^+ cations start to become a bit disordered, resulting in partially ordered MA^+. The cubic phase is found at high temperatures (above 330K) with the *Pm-3m* space group and is characterized by fully disordered MA^+ cations in the crystal structure. The disorder of the MA^+ cations increases with increasing temperature, meaning that their position becomes less well-defined in the crystal structure of $MAPbI_3$. Despite this, out of all phases of $MAPbI_3$, the cubic phase is ideal for solar cell applications because of the high cubic symmetry, leading to higher efficiency of the device [34].

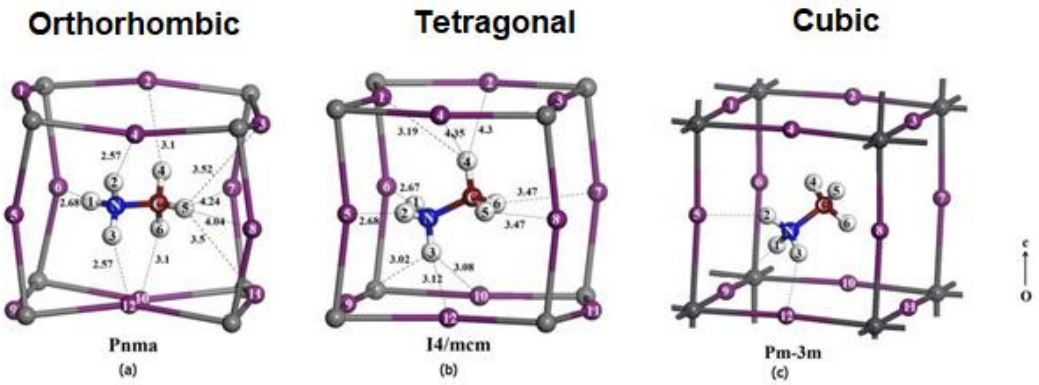

Figure 3: Phases of $MAPbI_3$ and the analysis of the chemical bonds between I (purple) and H atoms (white). (a) orthorhombic phase with a=8.98 Å and c=12.30 Å; (b) tetragonal phase with a=8.98 Å and c=12.57 Å; (c) cubic phase with a=b=c=6.455 Å. [32]

2.1.1 Effect of grain size and boundaries

The microstructure of the halide perovskite layer plays a crucial role in the performance of the solar cell with the size and boundaries of the crystal grains being important influences. As briefly mentioned in the introduction, halide perovskites typically form polycrystalline films due to the fast and uncontrollable crystal-growth (nucleation) kinetics of the perovskites. These films exhibit structural defects and small grain sizes, characterized by numerous grain boundaries. In this study, the focus is on epitaxial $MAPbI_3$ thin films. However, in epitaxial films, small crystal grain sizes and grain boundaries are still present. Figure 4 presents an AFM image of the epitaxial $MAPbI_3$, highlighting the presence of small grains, with an approximate grain size of 30 nm, and grain boundaries.

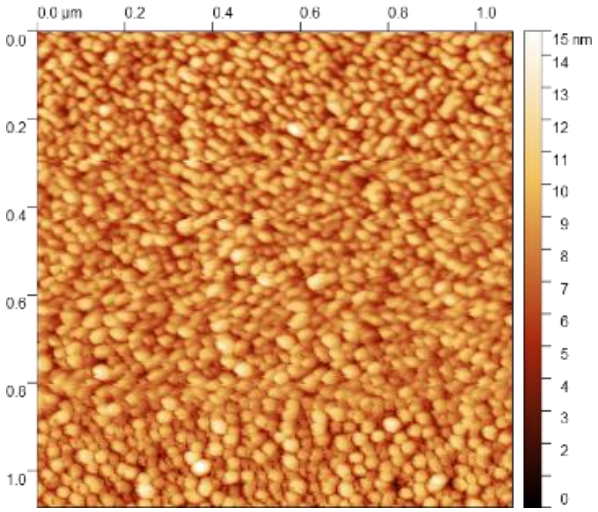

Figure 4: AFM image of epitaxial $MAPbI_3$ with apparent small grains and grain boundaries.

Researchers have found that micron-sized grains are more favourable in perovskites as it helps in charge carriers' separation and transport in the thin films [35]. Grain boundaries in a crystalline material disrupt the crystal's long-range periodicity causing electronic states to exist at energies that are prohibited in a bulk single crystal. These grain boundaries introduce various defects in the material such as chemical and vacancy segregation, dangling bonds and lattice dislocations, where carries can undergo recombination. [36]

By increasing the size of the grains, the density of the grain boundaries is reduced, thereby minimizing localized states where recombination can occur. Recombination means that the electrons and holes recombine together before travelling to their respective contact layers to generate photocurrent, therefore, reducing the charge extraction efficiency that is crucial for a high-efficiency solar cell. Additionally, grain boundaries can affect charge mobility, conductivity, and dielectric constant, while also acting as pathways for ion-migrations and moisture that lead to a fast degradation of the perovskite. [37]

Epitaxial $MAPbI_3$ thin films are already at an advantage over polycrystalline films because they have enhanced optoelectronic properties resulting from the ordered growth with a single orientation. However, increasing the grain size and lowering the grain boundaries is an effective way to further enhance the performance and solvent annealing has been an effective method to promote crystal grain growth [35].

2.2 Epitaxial growth via Pulsed Laser Deposition

As mentioned in the introduction, this study will rely on epitaxial $MAPbI_3$ thin films grown via PLD. Therefore, it is important to introduce both concepts together and how they are relevant.

Epitaxy is the ordered and oriented growth or deposition of a material on a substrate where the interface between the two lattices has a well-defined crystallographic relationship [38]. Hence, epitaxial films have one single crystal orientation, in comparison with polycrystalline films that have different random crystal orientations. There are two types: homoepitaxy, where the grown layers are of the same material as the substrate, and heteroepitaxy, where they both are of different materials. This very well-defined method of crystal growth on a substrate makes epitaxy very preferable for a wide range of advanced technologies such as optoelectronics as the quality of the thin films can be controlled with precision, leading to a uniform final structure with less defects [39]. One of the techniques used to grow epitaxial layers is Pulsed Laser Deposition (PLD).

PLD is a versatile technique used to grow epitaxial thin films, but not only, with precise control over the film stoichiometry and morphology [40]. It consists of an ultra-high vacuum (UHV) chamber, where the target material to be deposited and substrate are positioned inside. The target material is struck by a laser beam in a pulsed manner at a certain angle, where the material is vaporized as a plasma plume that deposits the ablated species on the substrate. Figure 5A shows a typical schematic of the PLD set-up. The epitaxial $MAPbI_3$ thin films that are used for solvent annealing are grown with the (001) crystal orientation via this method on a potassium chloride (KCl) substrate (Figure 5B).

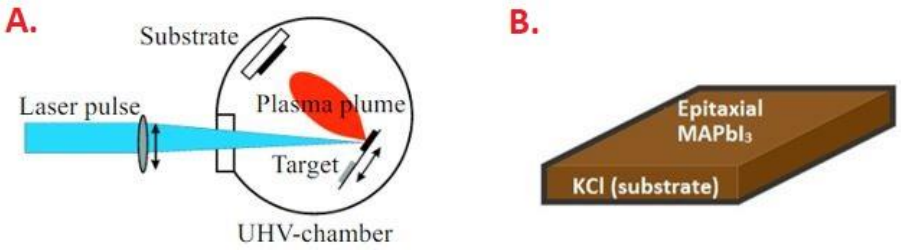

Figure 5: A. Schematics of a typical PLD set-up [40], B. Schematics of the epitaxial $MAPbI_3$ thin films employed in this study.

2.3 Optoelectronic properties of $MAPbI_3$

$MAPbI_3$ has attracted a lot of attention due to the remarkable optoelectronic properties. One crucial factor contributing to these properties is the band gap of the material. The band gap (E_g) is the energy difference between the valence and conduction bands, representing the minimum energy required for the electron to pass from the valence band to the conduction band [41]. It determines the range of light wavelengths that the material can absorb and emit, thereby affecting the optoelectronic properties. Understanding the band gap of the material is important as it provides insights into properties such as intrinsic carrier concentration, mobility of carriers, recombination mechanisms and excited state lifetime [41]. While this thesis does not extensively dive into exploring these properties, it aims to quantify the band gap and investigate how it is affected by solvent annealing.

The band gap of $MAPbI_3$ is relatively narrow with a value of approximately 1.6 eV within the visible light range, making it suitable for photon harvesting and preferable for solar cell applications [34,42]. Zhong et al. conducted calculations using density functional theory (DFT) with GGA-PBE and HSE06 functionals to determine the band structures for all phases of $MAPbI_3$ [42]. Among the functionals used, the GGA-PBE demonstrated better accuracy to experimentally calculated values. Figure 6 showcases the band structures of the cubic, tetragonal, and orthorhombic phases of $MAPbI_3$ as calculated using the GGA functional. It should be noted that DFT calculations can underestimate the actual value of the band gap.

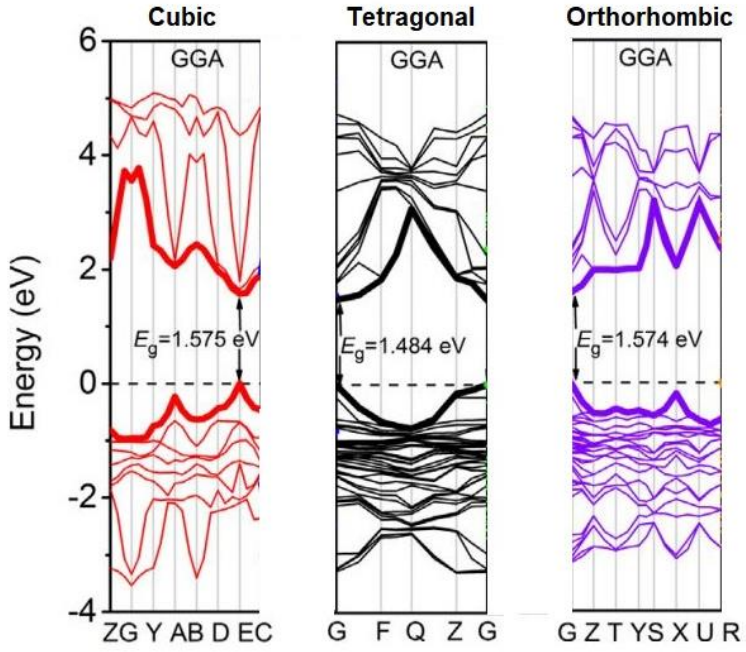

Figure 6: The band structures of the cubic, tetragonal and orthorhombic phases of $MAPbI_3$ calculated with the GGA-PBE functional. [42]

All phases of $MAPbI_3$ exhibit a direct band gap, with the momentum changing from one phase to the other. The specific values of the band gap differ between the phases, reflecting the structural variations. Notably, the cubic phase exhibits energy bands with the lightest effective masses among the three phases of $MAPbI_3$, as illustrated by the highly dispersed energy bands depicted in Figure 6. This indicates a higher carrier mobility within the cubic $MAPbI_3$ phase,

which makes this phase ideal for high performance devices [42]. These variations in band dispersion and effective masses have implications for the charge transport properties and overall optoelectronic performance of the different phases. In the context of this study, the cubic and tetragonal phases are of particular interest, as the orthorhombic phase occurs at very low temperatures.

2.4 Solvent annealing

Solvent annealing (SA) is a post-treatment technique that was introduced to enhance the perovskite crystallisation process. It was first proposed by Xiao et al. [24] and involves annealing the halide perovskite films while introducing a polar-aprotic solvent vapour, with commonly used solvents like dimethyl sulfoxide (DMSO) or dimethylformamide (DMF). SA has demonstrated remarkable improvements in perovskite film properties. It effectively reduces the density of grain boundaries and increases the grain size of perovskites up to 1μm [24-25], exceeding the maximum grain size (≈260 nm) in thermally annealed films [43]. Furthermore, SA films show improvement in properties such as increased charge recombination lifetime, reduced trap density, decreased charge extraction time and increased carrier diffusion length, which significantly enhances the final device performance [43]. Figure 7 shows a schematic of the SA treatment to increase the grain size of the $MAPbI_3$ thin films.

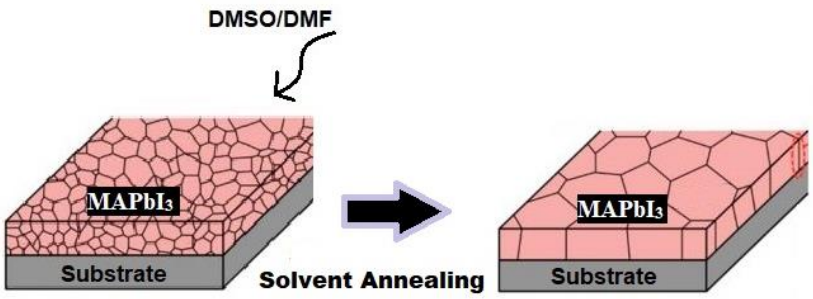

Figure 7: Schematics of the solvent annealing treatment to increase the grain size.

SA operates by introducing solvent molecules into the atmosphere during traditional thermal annealing. These solvent molecules preferentially reach areas of higher surface energy, particularly the grain boundaries within the perovskite thin film. At grain boundaries, they will penetrate the cubic octahedral perovskite structure, binding with organic molecules and initiating the formation of an intermediate phase crucial for perovskite crystallisation. At a certain temperature, the thermal equilibrium is reached between the entry and volatilization of the solvent molecules leading to the formation of the intermediate phase. This phase transition facilitates the fusion of adjacent grains, promotes the expansion of grain size, and contributes to the reduction of defect states within the material. [44]

In the SA treatment of the epitaxial $MAPbI_3$, only the DMSO solvent is tested. The DMSO vapour leads to the dissolution of the perovskite, creating a wet environment due to the high solubility of MAI and PbI_2 (precursors) in DMSO. In this way, the precursor molecules can diffuse more readily for longer distances because of the lower migration energy. DMSO coordinates with PbI_2 to form the MAI-PbI_2-DMSO intermediate phase because of the strong Lewis basicity attributed to the electron-donating methyl group of DMSO. Following the Ostwald ripening model, the dissolved precursor molecules undergo a process in which smaller

grains are re-deposited onto larger ones under the influence of surface energy. The intermediate phase of MAI-PbI_2-DMSO facilitates the redistribution and recrystallisation of the precursor molecules, contributing to the growth of larger and more structurally uniform $MAPbI_3$ grains. Therefore, in essence, SA is a dissolution-recrystallisation process. [45]

Regarding the specific chemical reaction mechanism involved in the dissolution of $MAPbI_3$ by DMSO, it remains uncertain due to limited definitive research on this topic. However, Yi et al. [46] suggested the chemical reaction below regarding solvent annealing with DMSO:

$$MAPbI_{3_{(solid)}} + DMSO_{(gas)} \rightleftharpoons MA_3PbI_5 \cdot (DMSO)_{(solid)} \; or \; MA_2Pb_3I_8 \cdot (DMSO)_{2_{(solid)}} + CH_3I_{(gas)} + NH_{3_{(gas)}}$$

2.5 Characterization techniques

In this section, the characterization techniques that are used to characterize the epitaxial $MAPbI_3$ thin films before and after solvent annealing are described. The thin films are characterized by X-Ray Diffraction (XRD), Atomic Force Microscopy (AFM) and Photoluminescence (PL) Spectroscopy.

2.5.1 X-Ray Diffraction

X-ray diffraction (XRD) is one of the most widely used techniques to characterize the crystal structure of materials. This characterization technique is fundamentally based on Bragg's Law, which establishes a relationship between the position of the peak in a diffraction pattern to the distance between atomic planes in a material [47]. Figure 8 illustrates Braggs diffraction of X-rays in a crystalline material, where X-rays of a particular wavelength interact with the regularly spaced atomic planes in a crystal and undergo diffraction. Figure 9 shows the set-up of XRD powder, which is also used for this research.

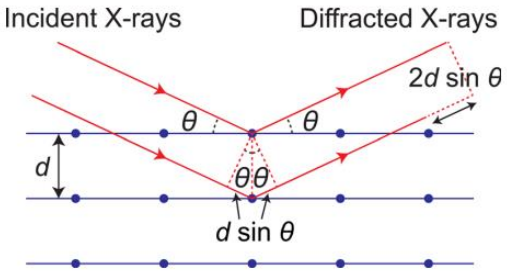

Figure 8: Braggs X-ray diffraction between atomic planes in a crystalline material. [47]

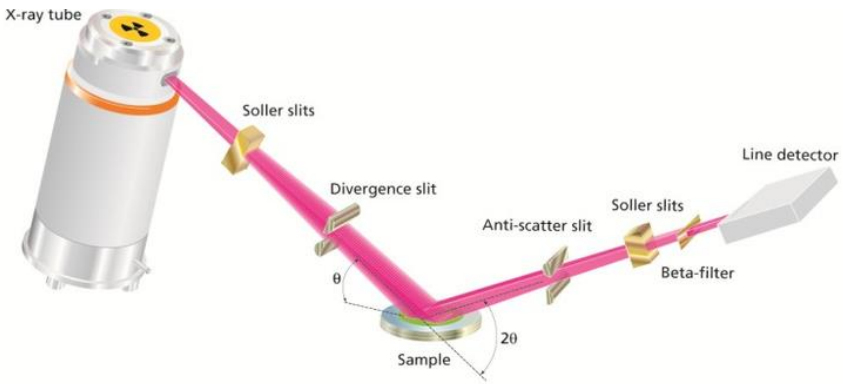

Figure 9: The set-up of the XRD powder measurements [48]. A copper (Cu) X-ray source with 1.54Å wavelength is used in this study.

According to the Bragg's law equation shown below, the interatomic spacing and the angle at which X-rays are diffracted are what determine the location of the diffraction peaks.

$$2d\ sin\theta = n\lambda$$

where d is the distance between atomic planes, θ is the angle between the incident X-rays and atomic plane, n is order of reflection and λ is the wavelength of X-rays.

XRD is of importance because you can extract valuable information such as the crystal structure, phase of the material and crystal plane orientation. In the context of this study, XRD is used to assess and confirm the crystal structure and orientations of the epitaxial $MAPbI_3$ thin films before and after solvent annealing. The changes in intensity and width of the peaks can provide insights into changes in crystallinity of the material that can be correlated to the effects of solvent annealing.

2.5.2 Atomic Force Microscopy

Atomic Force Microscopy (AFM) is a technique that allows the scanning and imaging of the surface structure with high accuracy and resolution down to the atomic scale. The fundamental principle of AFM is based on the interaction between a sharp probe tip and the sample. As the tip approaches the sample surface, the force between them is measured with a cuboid flat spring named cantilever. The surface contour is mapped while scanning along a constant z-axis, meaning that the tip-sample distance is kept constant. Figure 10 demonstrates a general AFM set-up. [49a]

.

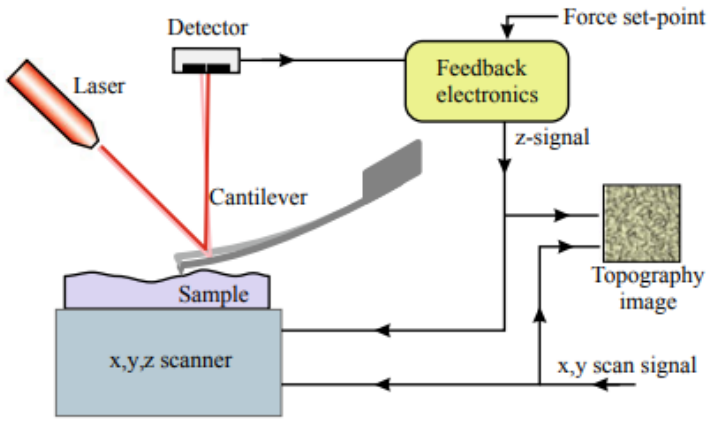

Figure 10: Schematics of a general AFM set-up. [49a]

There exist different modes of AFM such as contact, noncontact and tapping modes. This study employs the AFM Tapping mode, also known as Intermittent Contact mode. In the Tapping mode, the tip oscillates with a relatively large amplitude while intermittently making contact with the sample surface. The cantilever is excited at a constant driving frequency with the oscillation amplitude being measured. The tapping mode prevents instability in the feedback control of the tip-sample distance by having the amplitude depend monotonously on the tip-sample distance. Figure 11 shows a schematic of how the tip 'taps' onto the sample surface. [49b]

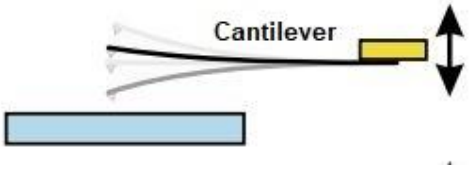

Figure 11: Schematic of the tip movements of the AFM Tapping mode. Adopted from [49b].

In this study, AFM Tapping mode will be used to provide a comprehensive surface analysis of the epitaxial $MAPbI_3$ thin films before and after solvent annealing. The focus will be on scanning and imaging the surface morphology, determining the average grain size and root mean square (RMS) surface roughness in order to assess the effects of solvent annealing on the structure of the thin films.

2.5.3 Photoluminescence Spectroscopy

Photoluminescence (PL) spectroscopy is a non-destructive and contactless technique for examining the electronic structure of materials by analysing the emission of the photons after the optical excitation of the material [50]. In PL spectroscopy, the material is excited using a light source (i.e. a 520nm excitation laser for this study) that gets absorbed. The electrons move from a low energy ground state (valence band) to a high energy excited state (conduction band). After a short time, electrons will gradually relax and move back to the ground state through radiative and non-radiative relaxation mechanisms. The radiative relaxation mechanism involves the emitting of photons, while the non-radiative mechanism results in an energy loss. These emitted photons are measured in the PL spectroscopy to characterize the energy band and optical properties of the material. Figure 12 shows the principles of the PL spectroscopy as described.

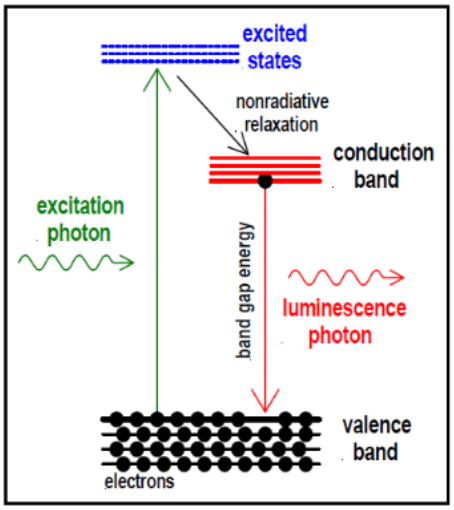

Figure 12: The principles of the PL spectroscopy. Adopted from [51].

PL spectroscopy is commonly divided into two main categories: steady-state PL and time-resolved PL. Steady-state PL is extensively employed and measures the luminescence under steady-state excitation conditions, typically in a defined wavelength range and continuous laser

source. In contrast, time-resolved PL measures the evolution of luminescence emission as a function of time. [52]

In this study, the steady-state PL is employed to investigate the band gap of the epitaxial $MAPbI_3$ thin films before/after solvent annealing and any potential changes or shifts in the final spectrum. The band gap of the material is quantified with the following equation:

$$E_g = \frac{hc}{\lambda}$$

where E_g *(J)* is the band gap energy (later converted in eV), h *(J×s)* is the Planck's constant, c *(m/s)* is the speed of light in vacuum and λ *(m)* is the wavelength corresponding to the maximum intensity in the PL spectrum.

Moreover, the full width half maximum (FWHM) is a key parameter used to analyse the PL peak. The FWHM represents the spectral width of the PL peak at half of its maximum intensity. A narrower FWHM indicates a narrower and well-defined emission, which is associated with higher material quality and a lower density of defects. On the other hand, a broader FWHM suggests wider energy distribution and increased presence of defects within the material. Therefore, by calculating the FWHM of the PL peak, information regarding the presence of defects and material quality can be obtained.

3. EXPERIMENTAL SETUP

This section provides a description of the materials utilized and the characterization instruments employed. Further, a detailed explanation of the solvent annealing procedure is presented, which compromises of SA method 1 and SA method 2.

3.1 Materials and characterizations

The details of the materials and equipment used are divided into bullet points.

- Epitaxial $MAPbI_3$ thin films
  - ➔ grown via PLD on a KCl substrate by the Optoelectronic research group of the University of Twente
  - ➔ 1x1 cm^2 thin films with a 70 nm thickness

- Solvent annealing procedure
  - ➔ DMSO solvent from Sigma-Aldrich with an anhydrous purity of >99.9%
  - ➔ Inside the N_2 glovebox: KIYON Nanovak glovebox

- Characterization techniques
  - ➔ XRD: Panalytical X'Pert Pro XRD instrument, Cu X-ray source with 1.54Å wavelength
  - ➔ AFM: Tapping in air mode using Veeco Dimension Icon AFM
  - ➔ PL: StellarNET INC Bluewave spectrometer, 520nm excitation laser from the MatchBox series, THORLABS FGL590S color filter

3.2 Solvent annealing procedure

The SA procedure can be divided into two methods, with the schematics shown in Figure 13. All experiments were performed inside the glovebox. The rationale behind employing two methods and the differences between them will be elaborated in the forthcoming 'Results and Discussion' section.

In Method 1, the epitaxial $MAPbI_3$ thin films are placed inside a petri dish. A specific quantity of the DMSO solvent is dropped near the sample in the form of a single drop. The petri dish is then covered on top, creating a sealed environment. The covered petri dish is placed on a hot plate set to a predetermined temperature. As the petri dish heats up, DMSO undergoes vaporization, transforming into a vapour that will penetrate the thin films. After a specified time, the thin films are removed from the hot plate and left to rest.

In Method 2, the procedure is similar to Method 1. The epitaxial $MAPbI_3$ thin films are placed inside a petri dish, and the DMSO solvent is dropped near the sample. The petri dish is covered and placed on a hot plate, allowing the DMSO to vaporize over time. However, in this method, the lid of the petri dish is removed after approximately 2-3 minutes, once the thin film has become transparent and DMSO has dissolved the $MAPbI_3$. The thin films are then removed from the hot plate on observing the colour change to dark brown.

The SA procedure parameters that have been investigated in this study include the time, solvent quantity, and temperature, with an emphasis on the solvent annealing time.

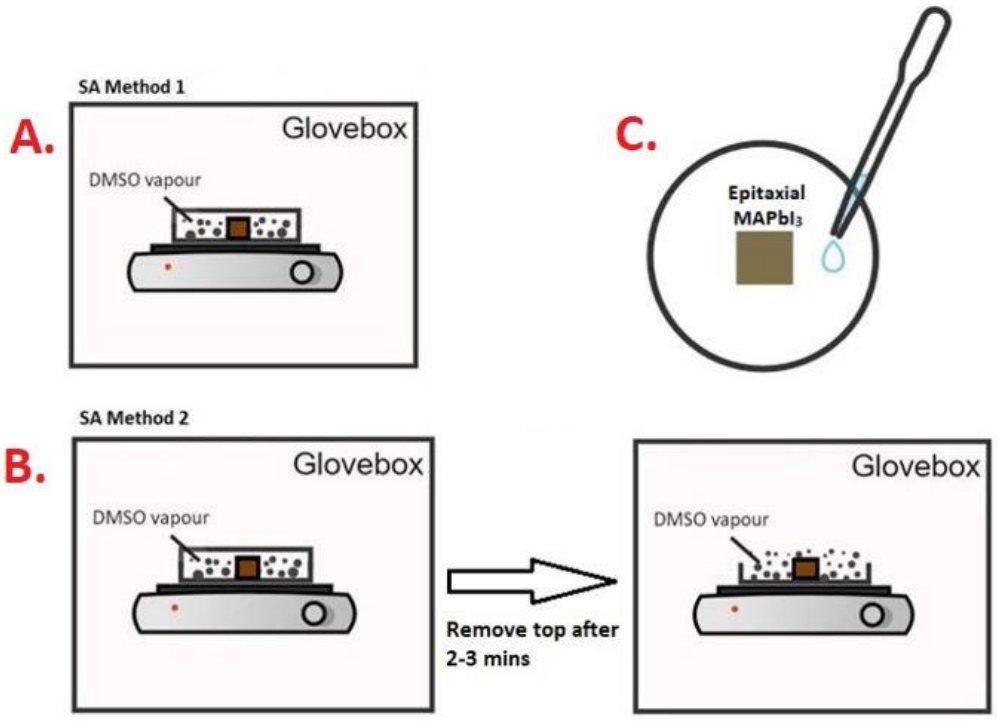

Figure 13: Schematics of the SA procedure. Schematic A. illustrates the set-up for SA Method 1, while schematic B. illustrates the set-up for SA Method 2. Schematic C. illustrates the set-up of the thin films inside the petri dish, which remains the same for both.

4. RESULTS AND DISCUSSION

In this section, the results and discussion of the SA experiments are presented. The focus is divided into two parts: SA Method 1 and SA Method 2. Initially, the experimental conditions and outcomes of SA Method 1 will be discussed, followed by a transition to a hypothesis and the results obtained from SA Method 2. These findings shed light on the impact of different parameters to provide insights into the effectiveness of SA.

4.1 Solvent Annealing (SA) Method 1

In this subsection, the results and discussion of the experiments done under the SA Method 1 are presented. The time, solvent quantity, and temperature parameters are examined to evaluate their influence on the epitaxial $MAPbI_3$ thin films.

However, before diving into the results, it is crucial to address the colour change exhibited by the epitaxial $MAPbI_3$ thin films during the SA treatment. Figure 14 displays the colour change that the thin films undergo during the SA treatment over time.

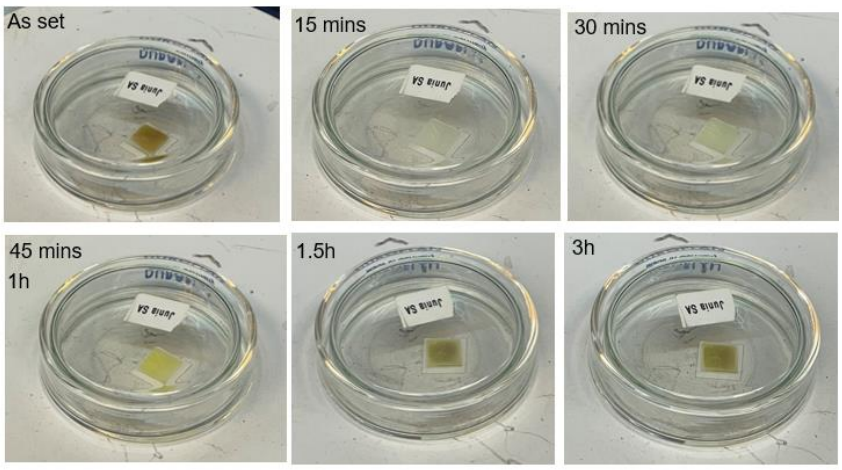

Figure 14: The color change of the epitaxial 70nm thick $MAPbI_3$ films during the SA treatment. The timestamps are depicted in each image.

Initially, the epitaxial $MAPbI_3$ thin films possess a distinctive brown colour, which can be attributed to the colour of $MAPbI_3$ perovskite. However, as the DMSO solvent vapour dissolves the $MAPbI_3$, the thin films become transparent. This transparency signifies the dissolution of the original perovskite phase. As the SA procedure progresses further, the thin films undergo a reformation process, leading to the re-emergence of the perovskite phase, which is indicated by the reappearance of the brownish colour. Thus, the observed colour change serves as a useful indicator to determine the point to conclude the SA treatment, as the desired brown colour reflects the formation of the $MAPbI_3$ perovskite phase. However, while this colour change serves as an initial indicator, it is not sufficient to conclude the perovskite formation and the characterization techniques are used to further confirm the perovskite formation.

In the forthcoming sub-sections, the different parameters namely time, solvent quantity and temperature are examined separately to understand the influence of SA method 1 on the epitaxial $MAPbI_3$ thin films.

4.1.1 Time parameter

Table 1 presents the summary of the SA experiments conducted with varying times, while keeping the other SA parameters the same. The initial experimental conditions were selected based on literature [24,45]. A temperature of 100°C was selected as it is commonly used for SA of halide perovskites. In consideration of the thickness of our epitaxial $MAPbI_3$ samples, a solvent quantity of 2.5 µL was used for 70 nm thick films. This adjustment was made to account for the discrepancy in thickness compared to the typically thicker samples (300-500 nm) used in other studies. The selection of the SA time for the first sample, 1.5 hours, was determined based on the observed colour change during the SA procedure. Specifically, the samples reverted to a brownish colour after 1.5 hours only, indicating the recrystallisation of the $MAPbI_3$. From there, longer (5h) and intermediate (3h) durations were chosen to investigate.

Name	Solvent	Temperature	Solvent quantity	Time
Sample 1	DMSO	100°C	2.5 µL	1.5 h
Sample 2	DMSO	100°C	2.5 µL	3 h
Sample 3	DMSO	100°C	2.5 µL	5 h

Table 1: Overview of the experimental conditions of the SA treatment with varying times.

Structural properties: XRD analysis

Figure 15 shows the XRD pattern for Sample 1, 2 and 3, each subjected to different SA times, presenting the results for the sample before solvent annealing (BSA), after solvent annealing (ASA) and the bare KCl substrate. In addition, reference patterns for the cubic phase, tetragonal phase, and precursors (PbI_2 and MAI) of $MAPbI_3$ are included.

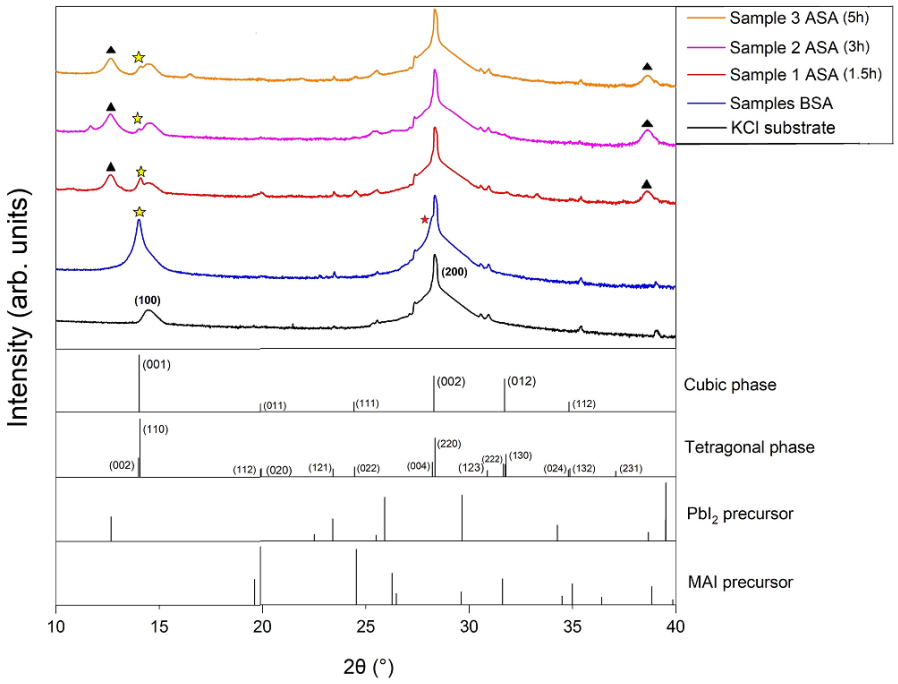

Figure 15: XRD result of Sample 1, 2, 3 with the respective SA time depicted in the legend. The black triangle depicts the PbI_2 precursor peaks and the yellow star depicts the perovskite phase peak. The red star depicts the (002) cubic phase peak for the samples BSA.

The KCl substrate contributes to the presence of certain peaks that are consistent across all samples. Specifically, the peaks at 14.5° and 28.3° correspond to the crystal orientations (100) and (200) of the KCl substrate, respectively. These substrate peaks are labelled in Figure 15 along the black line representing the KCl substrate XRD pattern.

In samples before SA, two important peaks are observed. The peak around 14°, marked by a yellow star, corresponds to the (001) orientation of the cubic phase peak of $MAPbI_3$. This peak is in very close proximity with the substrate's (100) orientation peak, observed as the shoulder on the right of the (001) cubic phase peak. Additionally, the peak at 28.3° corresponds to the (200) characteristic peak of the KCl substrate. However, in this case, it is in very close proximity with the (002) orientation peak of the cubic phase, as indicated by the small shoulder to the left of the substrate peak marked with a red star. These observations confirm the epitaxial nature of the $MAPbI_3$ thin films, exhibiting a cubic structure with a highly preferred orientation along the (001) crystal orientation.

Sample 1 ASA, treated for 1.5h, exhibits distinct peaks at 12.7° and 38.6°, which are attributed to the presence of the PbI_2 precursor (marked by a black triangle), in addition to the peaks originating from the substrate and the (001) cubic phase (marked by a yellow star). However, identifying the exact nature of the low-intensity peaks at 19.9° and 24.4° presents a challenge. Since these peaks closely align with the reference patterns of the cubic phase, tetragonal phase, and MAI precursor, it makes it difficult to determine their specific origin. It is suggested that the peak at 19.9° corresponds to the MAI precursor, supported by the presence of the PbI_2 precursor as it indicates that the precursors of $MAPbI_3$ are existing separately in the thin films, not together in the perovskite phase. The presence of the peak at 19.9° exclusively in Sample 1, without its observation in Sample 2 or 3, further suggests that it could correspond to the MAI precursor rather than the cubic or tetragonal phases of $MAPbI_3$. These findings indicate the possible decomposition of the perovskite and the escape of MAI from the thin film surface during SA over time.

Furthermore, the peak at 24.4° is proposed to correspond to the (022) orientation of the tetragonal phase. This indication is based on the calculated band gap value of 1.62 eV for Sample 1 that aligns with the reported band gap values for the tetragonal phase of $MAPbI_3$. This will be further discussed in the PL results section below. The possible coexistence of the cubic and tetragonal phases in the thin films after SA suggests that the peak at 14°, marked with a yellow star in the ASA samples, cannot be definitively identified as the (001) cubic phase peak anymore. Therefore, in this study, it will be referred to as the ‘perovskite phase peak’. Additionally, a peak at 33.3° remains unidentified as it does not correspond to any of the reference patterns utilized in the analysis.

With an increase in the SA time to 3h for Sample 2, a new peak emerges at 11.6° which can potentially be associated with lower-dimensional perovskites (2D) as it is found at low diffraction angles [53]. However, in the case of Sample 3 treated for 5h, the peak at 11.6° disappears, with a new unidentified peak at 16.4° appearing that does not align with any of the reference patterns utilized in the analysis.

The presence of PbI_2 precursor in all three samples ASA indicates incomplete conversion to the desired perovskite phase during the SA process. The intensity of the PbI_2 precursor peaks increases from Sample 1 to Sample 3, indicating an increase of the PbI_2 content over time. In contrast, the intensity of the perovskite phase peak is higher in Sample 1, indicating the

formation of the perovskite phase before 1.5h of SA treatment. As the SA treatment progresses over time, the intensity of the perovskite phase peak decreases, indicating degradation of $MAPbI_3$ to the precursors. Furthermore, the XRD analysis suggests a potential coexistence of the tetragonal and cubic phases after the SA treatment, indicating a loss of epitaxy, resulting in a polycrystalline structure.

Morphology: AFM analysis

Figure 16 presents the AFM results of a 5x5µm area for the samples before SA (BSA) and Sample 1, 2, and 3 after SA (ASA). Further, Figure 17 displays the AFM results of a 1x1µm area for Sample 1 BSA, which serves as a representative of the samples before the SA treatment, as well as Sample 1, 2, and 3 ASA. The surface roughness (RMS) is depicted in each image for the 1x1 results. These images provide a visual comparison of the morphological characteristics of the samples under different treatment conditions. Supplementary images of Sample 1 and 2 BSA (1x1) can be found in the appendices (chapter A).

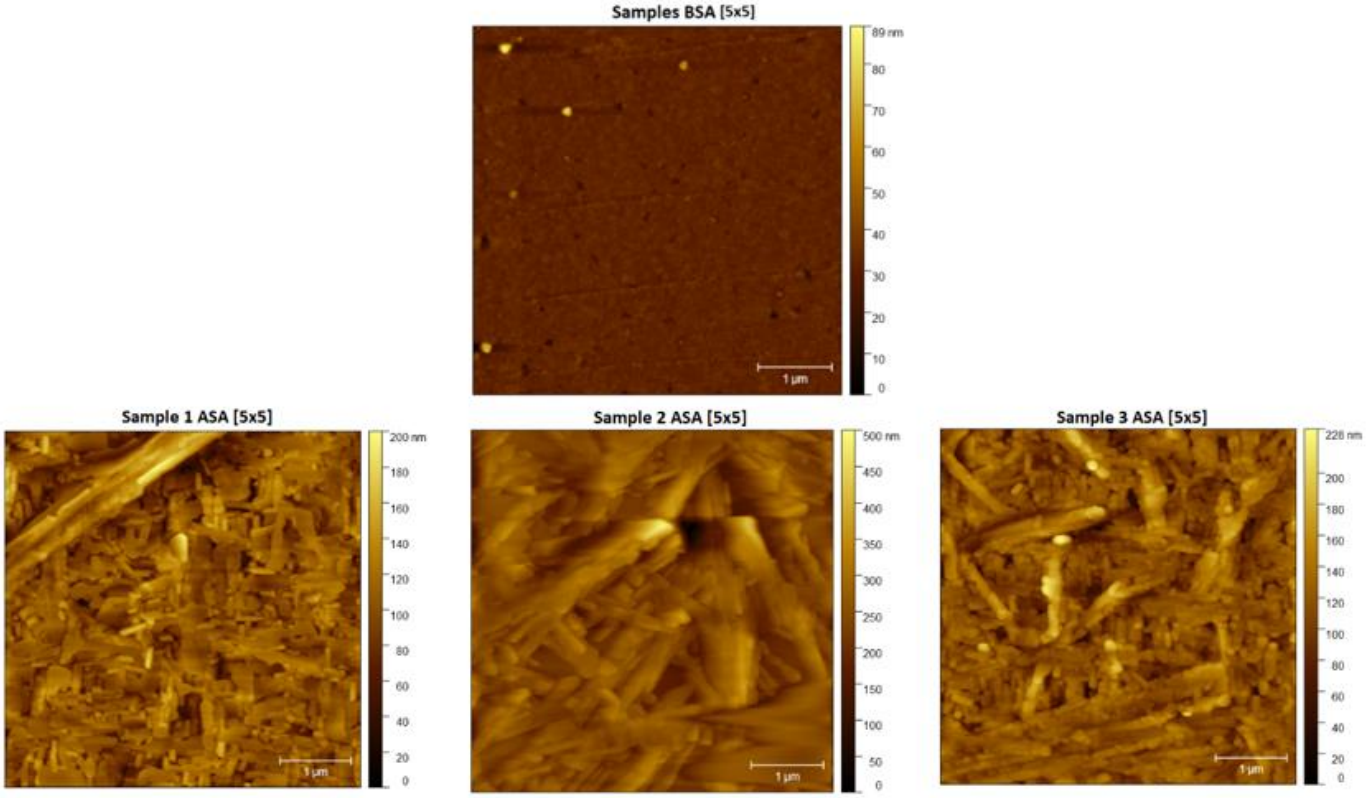

Figure 16: AFM 5x5 images of the Samples before solvent annealing (BSA) and Sample 1,2 and 3 after solvent annealing (ASA). AFM drift is present in all samples ASA.

The average grain sizes for Sample 1, 2, and 3 BSA are measured to be 31.5 nm, 40.5 nm, and 34.5 nm, respectively. Upon comparing the ASA images for the three samples, both the 5x5µm and 1x1µm images display similar morphologies. The AFM images of the SA samples show a lack of continuous and uniform grain structures, making it difficult to accurately measure the grain size. Notably, the 5x5 samples ASA images reveal the formation of rod-like structures that are not observed in the BSA samples. These structures are attributed to the excess PbI_2 precursor as confirmed by the increasing intensity of this precursor over time in the XRD results. Additionally, the 1x1 images in Figure 17 exhibit larger grain-like structures, which are likely associated with PbI_2. However, the exact nature of these structures cannot be definitively

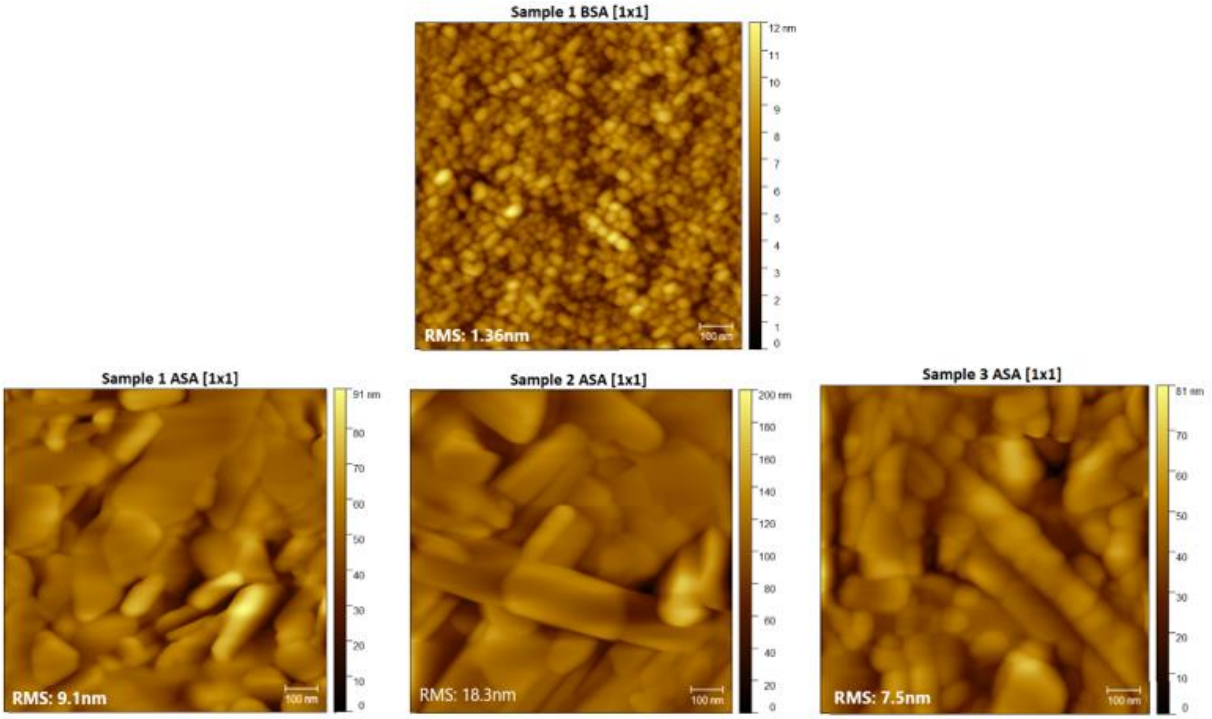

Figure 17: AFM 1x1 images of the Samples before solvent annealing (BSA) represented by Sample 1 BSA, and Sample 1,2 and 3 after solvent annealing (ASA). AFM drift is present in all samples ASA, however, a trend of larger grains is present.

determined without more advanced techniques that can provide deeper insights into their composition. Furthermore, the RMS values indicate an increasing trend in surface roughness for all the ASA samples compared to their BSA images. Nevertheless, a common trend among all the samples ASA is the presence of larger grains, indicating that the SA process does indeed contribute to grain size enhancement.

Optical properties: PL spectroscopy analysis

Figure 18 displays the PL results of the BSA and ASA samples, with ASA measured after 5, 10 and 15 mins. The normalized PL intensity results can be found in the appendices (chapter C), while Table 2 shows the calculated band gap and FWHM for both BSA and ASA samples. The PL intensity is plotted against both wavelength and energy axes. The energy (eV) of the peak corresponding to the maximum intensity signifies the band gap of the $MAPbI_3$ under different experimental conditions, labelled in each image.

A consistent observation across all ASA samples is a slight decrease in the band gap from 1.64 to 1.62 eV, as evidenced by the shift in the PL peak location (in eV) compared to BSA samples. This decrease in band gap is accompanied by a red shift in the PL spectrum when plotted against wavelength. The red shift means that the location of the peak for ASA samples in comparison with the BSA samples is moving to the right towards longer wavelengths in the PL spectrum, emitting lower energy photons, which aligns with the decrease in band gap. Furthermore, Table 2 demonstrates that FWHM of the ASA samples decreases over time and is lower than that of the BSA samples. This reduction in FWHM suggests a decrease in defects and a more well-defined and uniform shape of the PL peak.

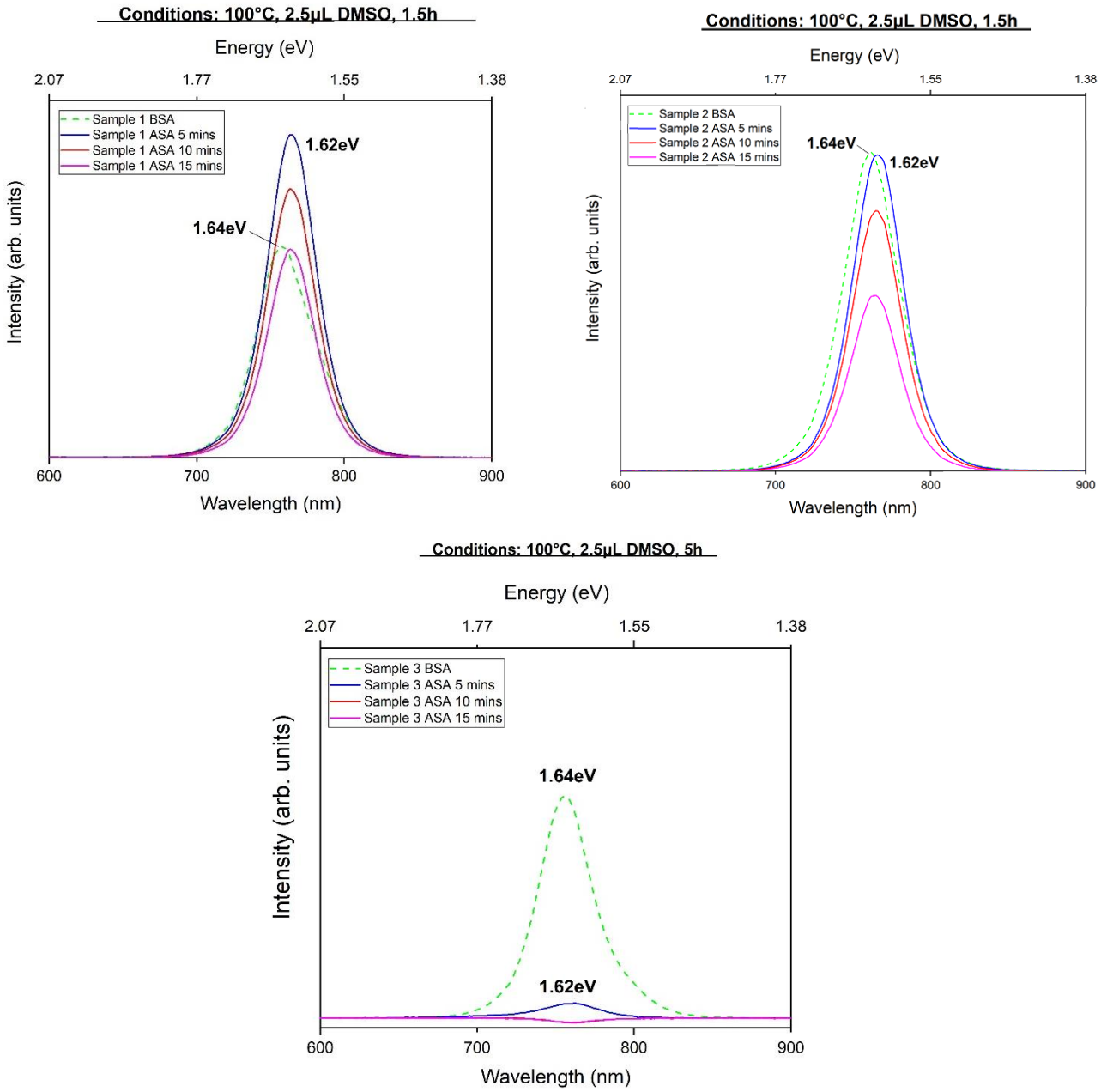

Figure 18: PL results for sample 1,2,3 ASA. The ASA samples are measured after 5,10 and 15 minutes. The SA conditions for each sample is depicted on top of the images, together with the peak location in eV labeled for each BSA and ASA peaks.

Name	**Band gap (BSA)**	**Band gap (ASA)**	**PL peak FWHM (BSA)**	**PL peak FWHM (ASA)**		
				After 5 mins	**After 10 mins**	**After 15 mins**
Sample 1	1.64 eV	1.62 eV	45.5 nm	38.5 nm	38 nm	37.5 nm
Sample 2	1.64 eV	1.62 eV	42.5 nm	38.5 nm	38 nm	37.5 nm
Sample 3	1.64 eV	1.62 eV	39.5 nm	42 nm	-	-

Table 2: The calculated BSA/ASA band gaps and PL peak FWHM of the Sample 1, 2 and 3.

In terms of PL intensity, a consistent decrease is observed over time for all ASA samples. This decrease in intensity can be attributed to the presence of an excess amount of PbI_2 precursor compared to the $MAPbI_3$ perovskite phase. When comparing Sample 1 ASA with a shorter SA time of 1.5h to Sample 3 ASA with a longer SA time of 5h, a more significant decrease in PL intensity is observed in Sample 3. This observation aligns with the increased intensity of the PbI_2 XRD peak observed in Sample 3 ASA, suggesting that the large excess of PbI_2 may be quenching the PL signal and leading to a decrease in intensity. The low conversion of the perovskite phase can also play a role in the decreased intensity of the samples ASA. Furthermore, in Sample 3 ASA, there is an observation of the PL peak being shifted upside down after 10 and 15 minutes of measurement. This is attributed to a measurement error in capturing the dark spectrum, resulting in negative peaks, and therefore, these data points cannot be included in the analysis.

The observed red shift in the PL spectrum can be attributed to structural changes in the $MAPbI_3$ thin films during the SA process. One important and common structural change observed in all ASA samples is the peak at 24.4° in the XRD results, which has been proposed to correspond to the (022) tetragonal phase peak. In Table 2, we observe a trend of the band gap values of the samples decreasing from 1.64 to 1.62 eV. These values align with the reported values in literature for each phase. Quarti et al. [54] reported experimental band gap values of 1.61 eV for the tetragonal phase and 1.69 eV for the cubic phase, with the cubic phase having higher band gap values. This indicates the potential coexistence of the tetragonal and cubic phases of $MAPbI_3$ after SA. The decrease in band gap and the presence of the 24.4° peak in the XRD, suggests that the red shift is possibly attributed to the coexistence of the cubic and tetragonal phases of $MAPbI_3$.

Among the three samples with different SA times, Sample 1 at 1.5 hours of SA shows the best results out of the three. Sample 1 demonstrates the lowest intensity of PbI_2 peaks and the highest intensity of the perovskite cubic phase of $MAPbI_3$, indicating a higher degree of conversion to the desired perovskite phase. PL results reveal a band gap of 1.62 eV, indicating the potential coexistence of the cubic and tetragonal phases and a decrease in PL intensity after SA attributed to excess PbI_2 precursor quenching the signal. However, the presence of discontinuous grains and an excess of PbI_2 suggest the need for further optimization in order to achieve the desired morphology and minimize the precursor content.

4.1.2 Solvent quantity parameter

After exploring the influence of SA times on the epitaxial $MAPbI_3$ thin films, the next parameter under investigation is the solvent quantity. In this section, we focus on Sample 4, which is subjected to the same conditions as Sample 1, with the exception of a decreased solvent quantity. This adjustment is made based on the hypothesis that excessive DMSO content in the SA process may affect the recrystallization of the $MAPbI_3$ precursors and hinder the complete formation of the desired perovskite phase.

Structural properties: XRD analysis

Sample 4 undergoes the SA process under the following conditions: 100°C, for 1.5 hours, and a reduced solvent quantity of 1 µL of DMSO. Figure 19 shows the XRD result for Sample 4 BSA and ASA with the appropriate reference patterns.

The XRD result of Sample 4 is very similar to the previous samples. In Sample 4 ASA, the PbI_2 precursor peaks at 12.7° and 38.6° are still present, exhibiting even higher intensities compared to the previously discussed samples. The perovskite phase peak at 14° is also observed, although with very low intensity. Furthermore, Sample 4 also exhibits the peaks at 19.9° and 24.4°. As discussed in previous samples, the peak at 19.9° is suggested to correspond to the MAI precursor, while the peak at 24.4° is proposed to be associated with the (022) tetragonal phase of $MAPbI_3$. This observation suggests the potential coexistence of the cubic and tetragonal phases in Sample 4, indicating that epitaxy is not preserved in this sample as well.

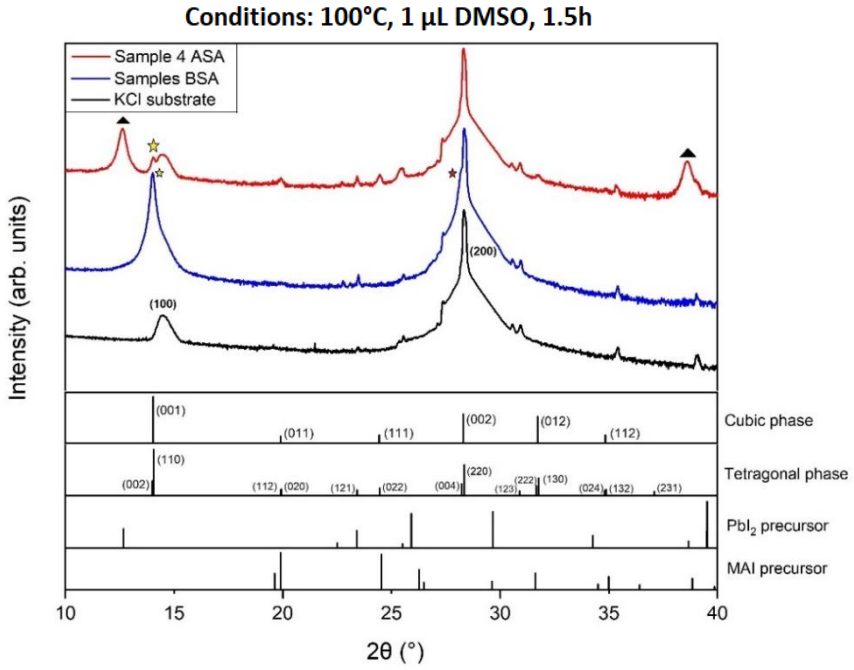

Figure 19: XRD result of Sample 4. The black triangle depicts the PbI_2 precursor peaks and the yellow star depicts the perovskite phase peak. The red star depicts the (002) cubic phase peak for the samples BSA.

Morphology: AFM analysis

Figure 20 showcases the 1x1 µm area AFM images of Sample 4 BSA and ASA, providing insights into the morphology of the sample. The 5x5 AFM image of Sample 4 ASA can be found in the appendices (chapter A). The RMS values increase from 1.3 to 13.5 nm, indicating an increase in surface roughness after the SA treatment. In terms of grain size, Sample 4 BSA has an average grain size of 34.5 nm.

However, the ASA image still presents challenges in accurately measuring the grain size of $MAPbI_3$ due to the absence of continuous, well-defined and uniform grain structures. In addition, although the AFM images display the presence of large grains, their exact nature cannot be definitively confirmed. Nonetheless, as previously discussed, these structures are likely attributed to the excess PbI_2 precursor, which is even more pronounced in Sample 4 when the solvent quantity is reduced (XRD peaks).

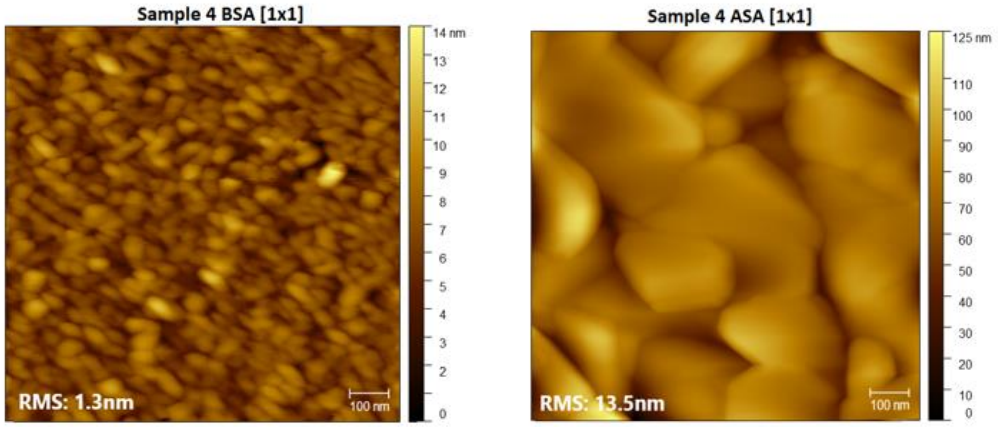

Figure 20: AFM 1x1 images of Sample 4 BSA and ASA. The RMS is depicted in each image. AFM drift is present in both the images, however, the increase in grain size is clear.

Optical properties: PL spectroscopy analysis

Figure 21 displays the PL result of Sample 4 BSA and ASA, for ASA measured at different time intervals (after 5,10 and 15 mins). The normalized PL intensity result can be found in the appendices (chapter C). Like the previous samples, Sample 4 ASA shows a decrease in band gap after the SA treatment with a decreased solvent quantity, with the peak position shifting from 1.64 to 1.62 eV. This decrease in band gap aligns with the observed red shift, where the PL peak shifts towards longer wavelengths, emitting lower energy photons. The decrease in band gap and the presence of the 24.4° peak in the XRD, suggests that the red shift is possibly attributed to the coexistence of the cubic and tetragonal phases of $MAPbI_3$. This is consistent with the previous samples results too.

The intensity of the PL peaks in the ASA sample is low, which can be attributed to the excess PbI_2 precursor, just like the samples discussed earlier. The excess PbI_2 may be quenching the PL signal and affecting the intensity. The low conversion of the perovskite phase could also be playing a role in the decreased intensity. As for the PL peak FWHM, it initially decreases from 46 nm in the BSA state to 38 nm in the ASA state, indicating a narrower and well-defined peak. However, over time, the FWHM of the ASA sample increases from 38 to 57.5 nm after 5 and 15 minutes, respectively. This suggests that the defects in the sample are increasing over time.

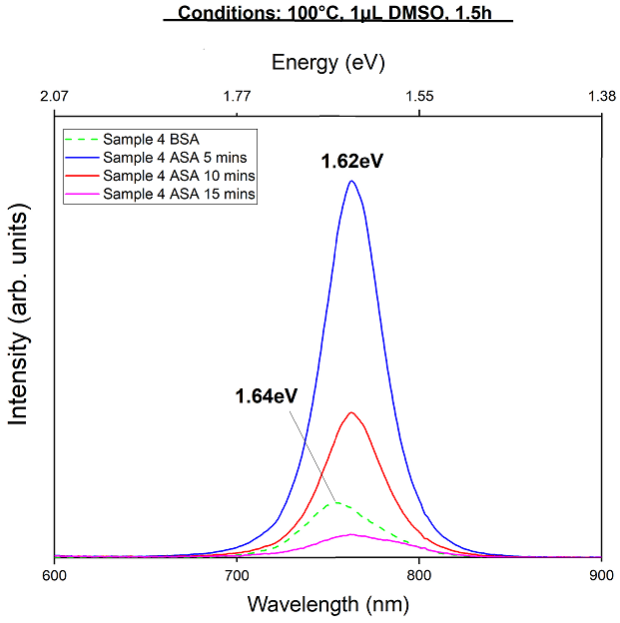

Figure 21: PL result for Sample 4 BSA and ASA. ASA is measured after 5,10 and 15 minutes.

After all the analysis of Sample 4, it is confirmed that that the reduction in solvent quantity in this sample did not result in an improvement compared to the previous samples. Instead, it led to a higher intensity of the PbI_2 precursor peak in the XRD spectrum and a slightly lower intensity of the perovskite phase peak. This could have possibly happened because of the DMSO reacting faster with a reduced solvent quantity, which results in faster perovskite decomposition to its precursors, with faster evaporation of the MAI precursor. This leads to the investigation of the temperature parameter to slow down the process and the rapid perovskite decomposition.

4.1.3 Temperature parameter

After exploring the influence of SA times and solvent quantity on the epitaxial $MAPbI_3$ thin films, the last parameter under investigation is the temperature. In this section, we focus on Sample 5, which is subjected to a lower SA temperature to potentially slow down the crystallisation process and mitigate the presence of excess PbI_2 and low conversion to the perovskite phase. The SA treatment for Sample 5 is carried out at a reduced temperature of 80°C, with a solvent quantity of 2.5 µL of DMSO, as the previous attempt to reduce the solvent quantity did not yield improvements, and with a duration of 6 hours. The SA process is conducted for a duration of 6 hours, representing the maximum time allotted in anticipation of a colour change to brown, which would indicate the perovskite formation. However, throughout the SA treatment, Sample 5 did not exhibit any significant colour change, suggesting that the reduction in temperature alone does not facilitate the conversion of precursors to the desired perovskite phase. The images depicting the colour of all the SA-treated samples can be found in the appendices (chapter B), revealing that Sample 5 displays minimal coloration compared to the other samples, indicating minimal to low formation of the perovskite phase.

Structural properties: XRD analysis

Figure 22 displays the XRD result for Sample 5 BSA and ASA, along with the corresponding reference patterns. The XRD analysis of Sample 5 presents a more perplexing and uncertain structure of the $MAPbI_3$ resulting from the SA treatment at decreased temperature of 80°C.

In Sample 5 ASA, the PbI_2 precursor peaks at 12.7° and 38.6° are still present, although with low intensities. The perovskite phase peak at 14° exhibits the lowest intensity among all the samples, indicating minimal conversion to the desired perovskite phase. The peak at 11.6°, as seen in Sample 2, suggests the potential existence of lower-dimensional perovskite structures (2D), as it is observed at low diffraction angles. Additionally, the peak at 26.4° corresponds to the MAI precursor, while the peak at 19.9° is also likely associated with the MAI precursor, as discussed in previous samples. However, Sample 5 exhibits several unidentified peaks at 13.2°, 21°, 24°, 33.3°, and 37.4°, further complicating the structural analysis. These ambiguities raise questions about the exact structure of this sample, which remains undetermined. Consequently, maintaining epitaxy in Sample 5 is uncertain.

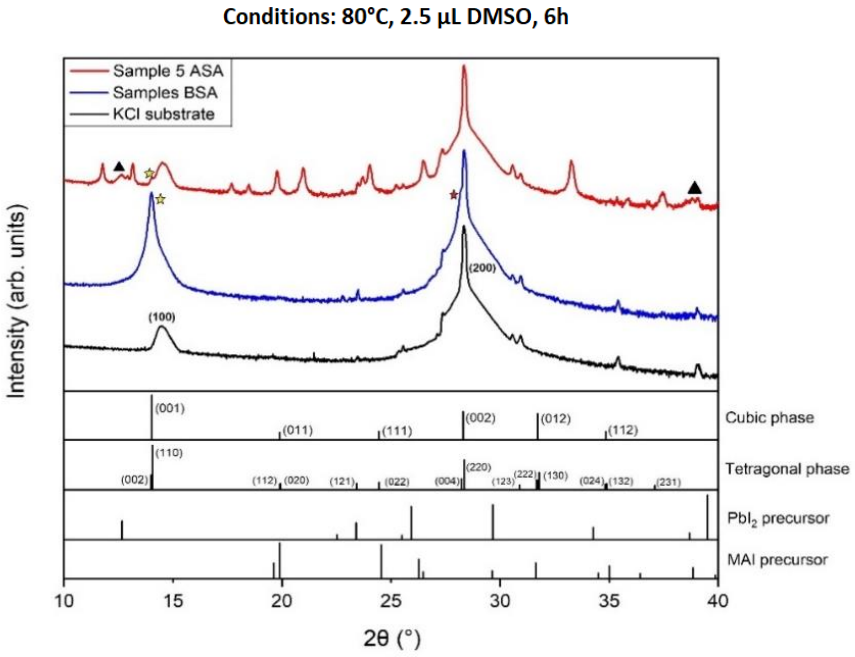

Figure 22: XRD result of Sample 5. The black triangle depicts the PbI_2 precursor peaks and the yellow star depicts the perovskite phase peak. The red star depicts the (002) cubic phase peak for the samples BSA.

Morphology: AFM analysis

Figure 23 showcases the AFM 1x1 images of Sample 5 BSA and ASA, while the 5x5 ASA image of Sample 5 can be found in the appendices (chapter A). The RMS value decreases from 3.3 nm to 717.4 pm, indicating a significant reduction in surface roughness. The average grain size for Sample 5 BSA is measured at 36.5 nm. However, in the AFM image of Sample 5 ASA, the presence of agglomerated small grains of $MAPbI_3$ is evident, and they do not cover the entire surface. This observation aligns with the XRD results, indicating a very limited conversion to the perovskite phase. Unlike the previous samples, there is no trend of larger grain formation observed in Sample 5 ASA. Furthermore, the 5x5 AFM image of Sample 5 ASA exhibits rod-like structures, similar to those observed in Figure 16, suggesting their association with the PbI_2 precursor. These findings provide further evidence of the limited perovskite conversion in Sample 5, which was treated with a lower temperature, indicating that insufficient thermal energy is provided for the complete conversion to the perovskite phase.

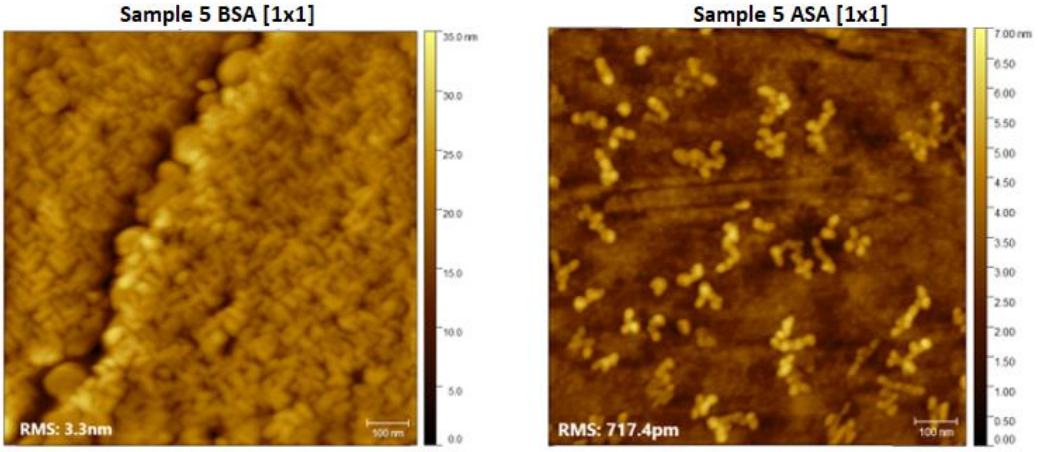

Figure 23: AFM 1x1 images of Sample 5 BSA and ASA. The RMS is depicted in each image. AFM drift is present in Sample 5 BSA.

Optical properties: PL spectroscopy analysis

Figure 24 shows the PL result of Sample 5 BSA and ASA, with ASA measured after 5, 10 and 15 mins. The normalized PL intensity result can be found in the appendices (chapter C). As observed in all the previous samples, Sample 5 ASA treated with a decreased temperature, demonstrates a decrease in band gap, with the PL peak location shifting from 1.64 to 1.62 eV. The red shift in the PL spectrum can be attributed to the structural changes that occur in Sample 5 ASA. However, due to the uncertainty in the structural analysis (XRD), it is challenging to determine the exact cause of the red shift. The possible coexistence of the cubic/tetragonal phases with a lower-dimensional (2D) perovskite phase, suggested by the presence of the peak at 11.6°, could contribute to the observed red shift. However, the presence of numerous unidentified peaks that do not align with the reference patterns complicates the structural interpretation. Further investigations are needed to determine the specific structural changes responsible for the red shift in Sample 5 ASA.

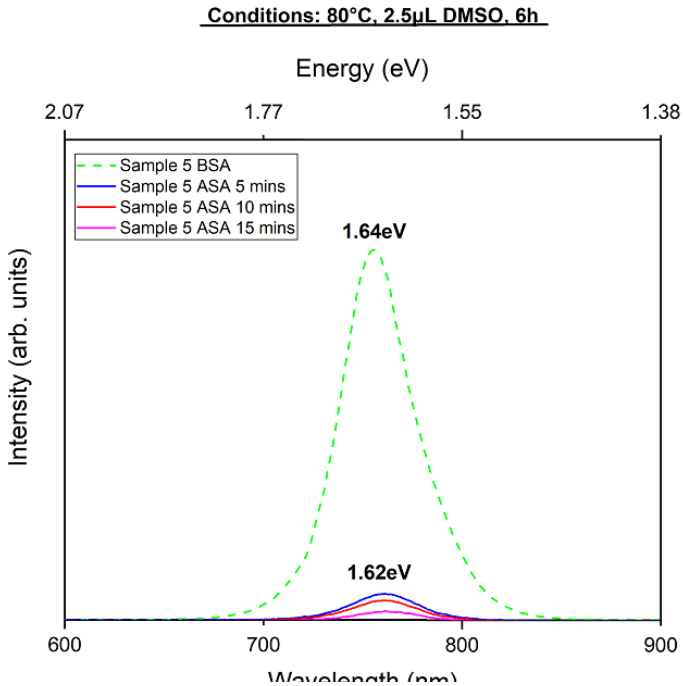

Figure 24: PL result for Sample 5 BSA and ASA. ASA is measured after 5,10 and 15 minutes.

The PL peaks in the ASA sample exhibit low intensity, which can be attributed to the presence of PbI_2 or MAI quenching the signal, as well as the minimal conversion of the perovskite phase. In terms of the FWHM, it decreases from 43 nm in the BSA sample to 38.5 nm in the ASA sample. Over time, the ASA sample shows a decreasing trend in the FWHM, measuring 38.5 nm, 37.5 nm, and 33 nm after 5, 10, and 15 minutes, respectively. This suggests a reduction in defects within the sample over time.

However, despite the adjustments in temperature, the analysis confirms that the decrease in temperature in Sample 5 did not result in an improvement compared to the previous samples. Although it led to a lower intensity of the PbI_2 precursor peak in the XRD pattern, it also resulted in the lowest intensity of the perovskite phase $MAPbI_3$ peak among all the samples.

4.2 Hypothesis

After the investigation of the SA parameters including time, solvent quantity, and temperature under SA method 1, it is evident that none of the samples yielded the desired results. The AFM images showed a lack of continuous, uniform, and large grains that were anticipated from the SA process. This can be attributed to the significant excess of PbI_2 precursor and lower conversion of the perovskite phase observed in the ASA samples, as indicated by the XRD/AFM results. However, in the AFM ASA images, a trend a larger grains is indeed present which raises questions about why the SA treatment did not yield the desired outcomes.

To gain further insights into the underlying causes of these observations, a reference sample is introduced. The reference sample underwent thermal annealing at 100°C for 1.5 hours without the presence of DMSO solvent, just as the SA conditions of Sample 1 which has the 'best' results among all five samples. Figure 25 displays the XRD, AFM, and PL results of the reference sample, which will be shortly commented on.

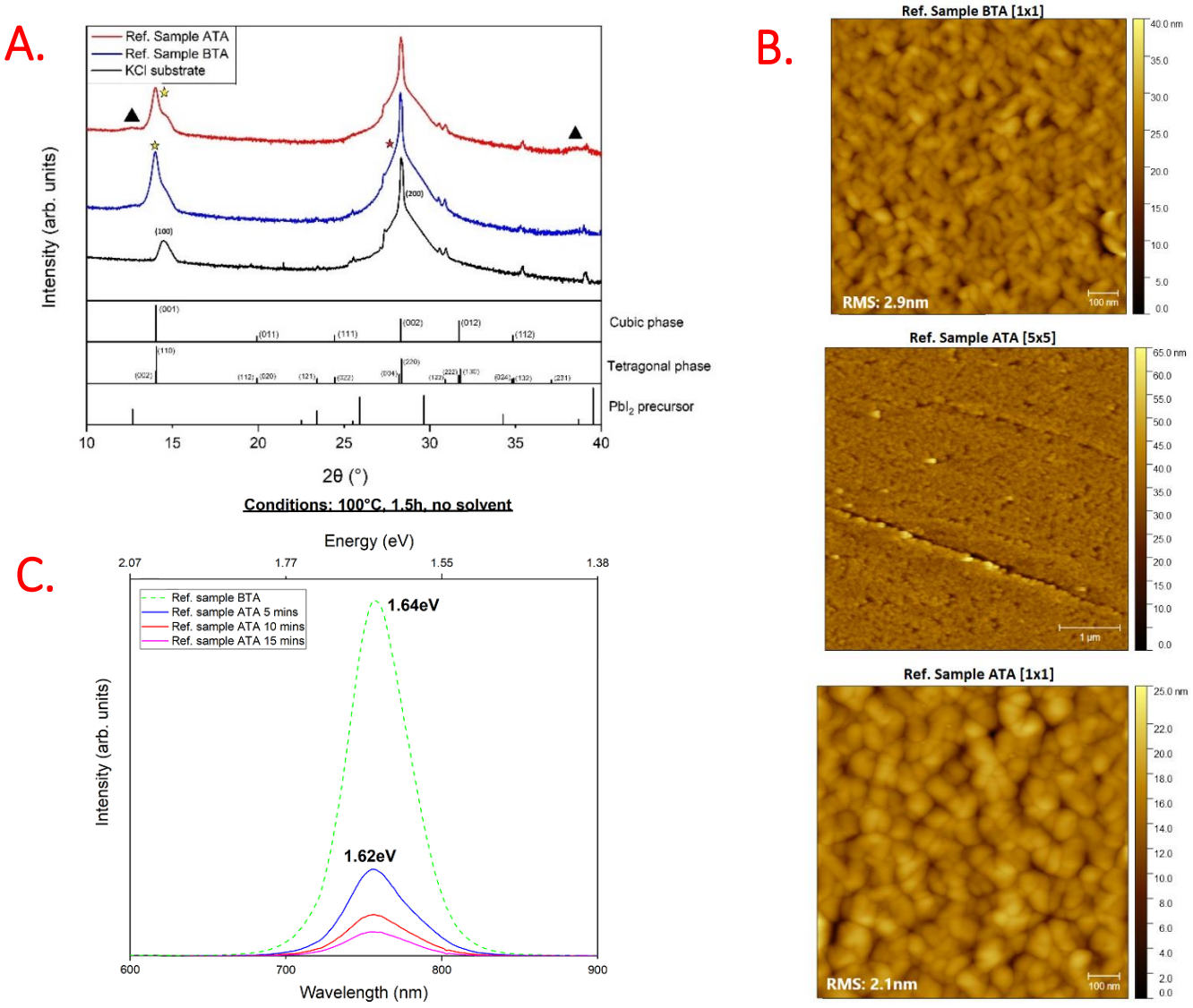

Figure 25: The XRD, AFM and PL results of the reference sample i.e., annealed without DMSO, where A. depicts the XRD pattern, B. the AFM images and C. the PL. BTA stands for before thermal annealing and ATA stands for after thermal annealing.

The AFM of the reference sample revealed an increase in grain size from 30 to 47.5 nm. This indicates that the specific temperature and duration of thermal annealing provides favourable conditions for grain growth, contrary to the results for Sample 1 which underwent SA. Moreover, the XRD results of the reference sample reveal low intensity peaks corresponding to the PbI_2 precursor, indicating very low excess of this precursor compared to the SA method 1 samples. Additionally, the perovskite phase peak exhibits higher intensity, which in this case it corresponds to the (001) cubic phase peak of $MAPbI_3$. This means that the epitaxy of the $MAPbI_3$ thin films is preserved with thermal annealing. The PL results show a red shift, with the band gap decreasing (PL peak shifting) from 1.64 to 1.62 eV. The observed red shift could be possibly attributed to the structural changes occurring in the reference sample, such as the increase in grain size or potential epitaxial strain relaxation towards the lattice substrate.

Based on these compelling results from the reference sample, it becomes apparent that the exposure to DMSO solvent plays a crucial role in decomposing the perovskite and hindering its reformation, resulting in the retention of excess PbI_2 precursor on the surface. Therefore, based on the reference sample findings and the observed trends in samples 1-5, a hypothesis is proposed.

The hypothesis suggests that over time, the perovskite undergoes decomposition, with the MAI precursor escaping or leaving the surface after reacting with DMSO. Figure 26 provides a schematic diagram illustrating this proposed phenomenon. Initially, as DMSO evaporates and reaches the surface of the $MAPbI_3$ thin films, it dissolves the films, converting them into liquid $MAPbI_3$. The transition to a transparent colour indicates that DMSO has already reacted on the surface, after which it begins to leave. The prolonged exposure to DMSO vapour, coupled with the high temperature of 100°C, triggers the thermal decomposition of the perovskite. Consequently, the MAI precursor gradually evaporates over time, leaving only the PbI_2 precursor on the surface. This explanation is consistent with existing literature, which indicates that the thermal degradation of $MAPbI_3$ commences at temperatures around 100°C [55]. As a result, $MAPbI_3$ decomposes into MAI and PbI_2, with the MAI evaporating over time and leaving the system while PbI_2 remains retained on the surface [55].

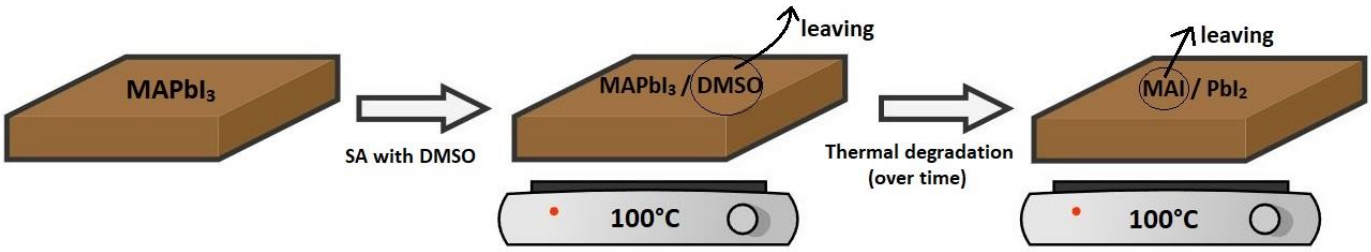

Figure 26: Schematic diagram of the proposed hypothesis.

The hypothesis is further supported by the findings from samples 1-5, which demonstrate a consistent trend in the XRD results. The XRD analysis reveals an increased intensity of the PbI_2 peaks and a decreased intensity of the perovskite phase peak as the SA treatment duration increases from 1.5 hours for Sample 1 to 5 hours for Sample 3. In addition, the peak at 19.9° that is suggested to correspond to the MAI precursor is evident in Sample 1 only, while for Sample 2 and 3 it does not show. This suggests a gradual evaporation of the MAI precursor over time, leading to a decrease in perovskite conversion and the retention of excess PbI_2 precursor on the surface.

Sample 4, where a decreased solvent quantity was employed, exhibited the highest intensity of the PbI_2 peaks among all five samples in the XRD results. This can be attributed to the more rapid evaporation and reaction of the smaller quantity of DMSO with the thin film surface. As a result, the MAI precursor escapes more quickly, leading to a higher intensity of the PbI_2 peak compared to Sample 1, which was treated for the same duration but with an increased solvent quantity.

Furthermore, the decreased temperature of 80°C with the prolonged exposure of 6h used in Sample 5 appears to be insufficient to provide the necessary thermal energy for complete perovskite transformation. This is evident from the lack of colour change in the ASA thin films during the whole SA treatment and the presence of both PbI_2 and MAI precursors in the XRD results. The DMSO effectively dissolved the precursors, but the insufficient thermal energy and extensive SA time, hindered their conversion back into the perovskite phase.

Based on these observations, it becomes apparent that the SA method 1 is not suitable for achieving the desired outcomes. The precise control of the SA parameters is crucial, especially the time parameter. Prolonged exposure increases the risk of thermal degradation, while rapid removal of DMSO after surface reaction is essential for unhindered complete perovskite formation. To address these challenges and improve the results, SA method 2 is introduced as an alternative approach which will follow in the next section.

4.3 Solvent Annealing (SA) Method 2

The SA method 2, detailed in Section 3.2, is employed as an alternative, optimized approach. It follows a similar procedure to SA method 1 with the epitaxial $MAPbI_3$ thin films placed inside a petri dish and DMSO solvent dropped near the sample. However, a crucial difference is that in SA method 2, the lid of the petri dish is removed after 2-3 minutes, once the thin film has become transparent and the DMSO has dissolved the $MAPbI_3$. By allowing the DMSO to vaporize without the confinement of the lid, the new method aims to promote more favourable conditions for perovskite formation and limit the long exposure of DMSO in the surface, which can lead to perovskite decomposition. Furthermore, the removal of the thin films from the hot plate only after the observed colour change to brownish serves as an indicator of successful perovskite conversion and helps prevent prolonged exposure to high temperatures, mitigating the risks of thermal degradation. Through the implementation of SA method 2, it is anticipated that the desired outcomes of continuous, uniform, and larger grains can be achieved, providing a more effective approach to increase the grain size.

Sample 6 and 7 are employed under SA method 2. Table 3 shows the experimental conditions for each of the samples, where the only changed parameter is the SA time. In this new method, shorter SA times of 10 minutes and 5 minutes were chosen to minimize the exposure of the thin films to DMSO and reduce the risk of perovskite decomposition, as described in the proposed hypothesis.

Name	**Solvent**	**Temperature**	**Solvent quantity**	**Time**
Sample 6	DMSO	100°C	2.5 µL	10 mins
Sample 7	DMSO	100°C	2.5 µL	5 mins

Table 3: Overview of the experimental conditions of the SA treatment under SA Method 2.

Structural properties: XRD analysis

Figure 27 presents the XRD results for Sample 6 and 7, which exhibit similarities to the previously discussed samples under SA method 1.

Both samples display the presence of PbI_2 precursor peaks at 12.7° and 38.6°, with Sample 7 showing higher intensities of these peaks compared to Sample 6. The intensity of the perovskite phase peak at 14° is more prominent in Sample 6 than in Sample 7. Both samples also exhibit peaks at 24.4°, although with low intensities, which were suggested to correspond to the (022) tetragonal phase of $MAPbI_3$. Additionally, Sample 7 displays an unidentified peak at 33.3°, as first observed in Sample 1, which does not match any of the reference patterns utilized. These observations suggest the potential coexistence of the cubic and tetragonal phases in Sample 6 and 7, indicating that epitaxy is not preserved in these samples as well.

Among all the samples, Sample 6 demonstrates the highest conversion to the perovskite phase and the lowest intensity of the PbI_2 peaks, suggesting an improvement over the samples under SA method 1. These observations already indicate that SA method 2 is showing more favourable outcomes, aligning with the proposed hypothesis.

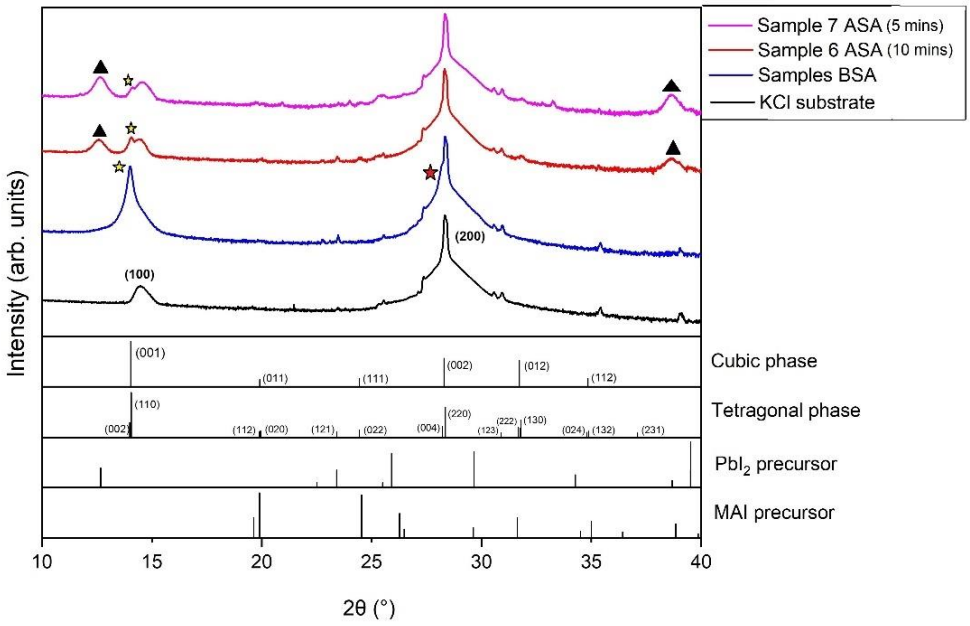

Figure 27: XRD result of Sample 6 and 7, with the respective SA time depicted in the legend. The black triangle depicts the PbI_2 precursor peaks and the yellow star depicts the perovskite phase peak. The red star depicts the (002) cubic phase peak for the samples BSA.

Morphology: AFM analysis

Figure 28 displays the AFM images of Sample 6 and 7 in both the BSA and ASA states, providing insights into the morphology of the samples. The 5x5 AFM images for Sample 6 and 7 ASA can be found in the appendices (chapter A). The RMS values, depicted in each image, indicate an overall increase in surface roughness following the SA treatment.

Sample 6 demonstrates a distinct improvement in the grains' morphology, showing continuous grains of $MAPbI_3$ throughout the surface. The grain size increases from 32.5 nm in the BSA state to 75 nm in the ASA state. This observation reaffirms the influence of the SA treatment on enhancing grain size. Moreover, the 5x5 image of Sample 6 ASA does not exhibit the

previously observed rod-like structures attributed to the excess PbI_2 precursor. This suggests a reduced presence of PbI_2 in the thin films, as supported by the XRD analysis.

In the case of Sample 7, the average grain size in the BSA state measures 30 nm. The 1x1 ASA image displays similarities to the morphology observed in previous samples, with the presence of large, continuous lines of 'grains' resembling rod-like structures, which can be attributed to the excess of PbI_2 and low conversion of the perovskite phase. This observation is further supported by the 5x5 ASA image of Sample 7, which clearly depicts these rod-like structures corresponding to the PbI_2 precursor. Although the average grain size in the ASA state cannot be accurately measured, there is a clear trend of larger grains compared to the BSA state, indicating the contribution of the SA treatment to grain size enhancement.

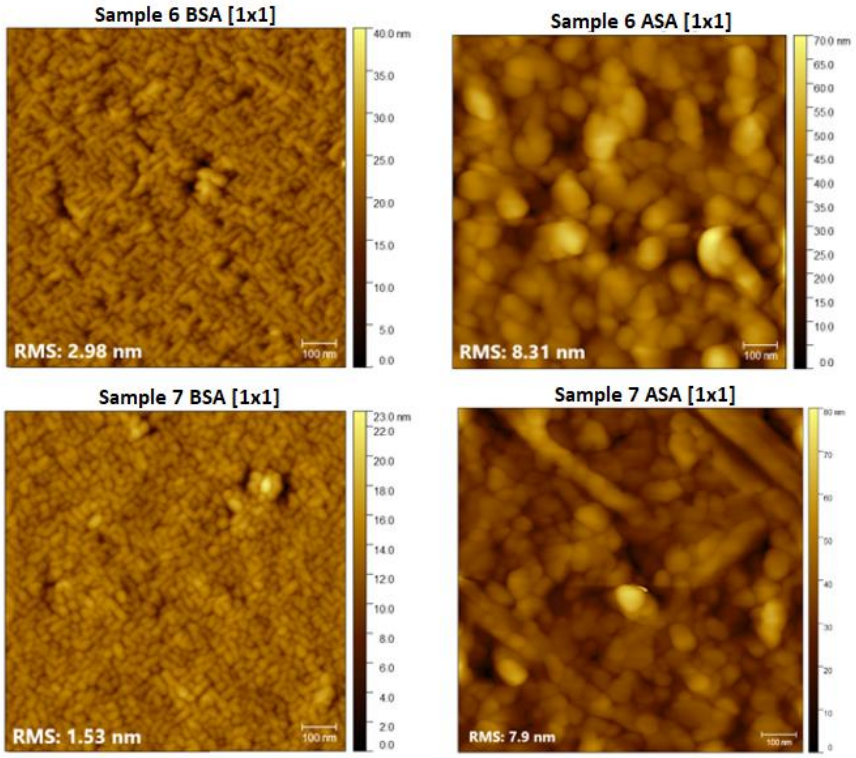

Figure 28: AFM 1x1 images of Sample 6 (10 mins of SA) and 7 (5 mins of SA) BSA and ASA. The RMS is depicted in each image. AFM drift is present in the images.

Optical properties: PL spectroscopy analysis

Figure 29 shows the PL results of Sample 6 and 7 BSA and ASA, with ASA measured after 5, 10 and 15 mins. The normalized PL intensity results can be found in the appendices (chapter C). Table 4 displays the calculated band gaps and FWHM values for each sample before and after SA.

Sample 6 ASA exhibits a decrease in band gap, with the peak position shifting from 1.64 to 1.62 eV. Similarly, Sample 7 also exhibits the same trend, with the band gap decreasing from 1.6 to 1.62 eV. Both of these samples show a red shift in the PL spectrum after the SA treatment. The presence of the 24.4° peak in the XRD results accompanied by the decrease in the band gaps of both samples, suggest that the red shift might be attributed to the (possible) coexistence of the cubic and tetragonal phases of $MAPbI_3$. Additionally, the FWHM values of the ASA

samples decrease over time, indicating a reduction in defects and a more well-defined peak shape.

In the case of Sample 6, the PL intensity for the ASA state is higher compared to the BSA state. Furthermore, the intensity of Sample 6 ASA increases gradually over the measured time period (from 5 to 15 mins). This is contrary to the commonly observed decrease in intensity for the previous ASA samples, as also observed in the PL spectra of Sample 7. The increase in the PL intensity in Sample 6 ASA may be attributed to the lower presence of PbI_2 precursor, as suggested by the XRD and AFM results, as well as a higher conversion to the perovskite phase. On the other hand, the decrease in PL intensity over time in Sample 7 can be attributed to the excess of the PbI_2 precursor, which can quench the PL intensity along with a lower conversion of the perovskite phase.

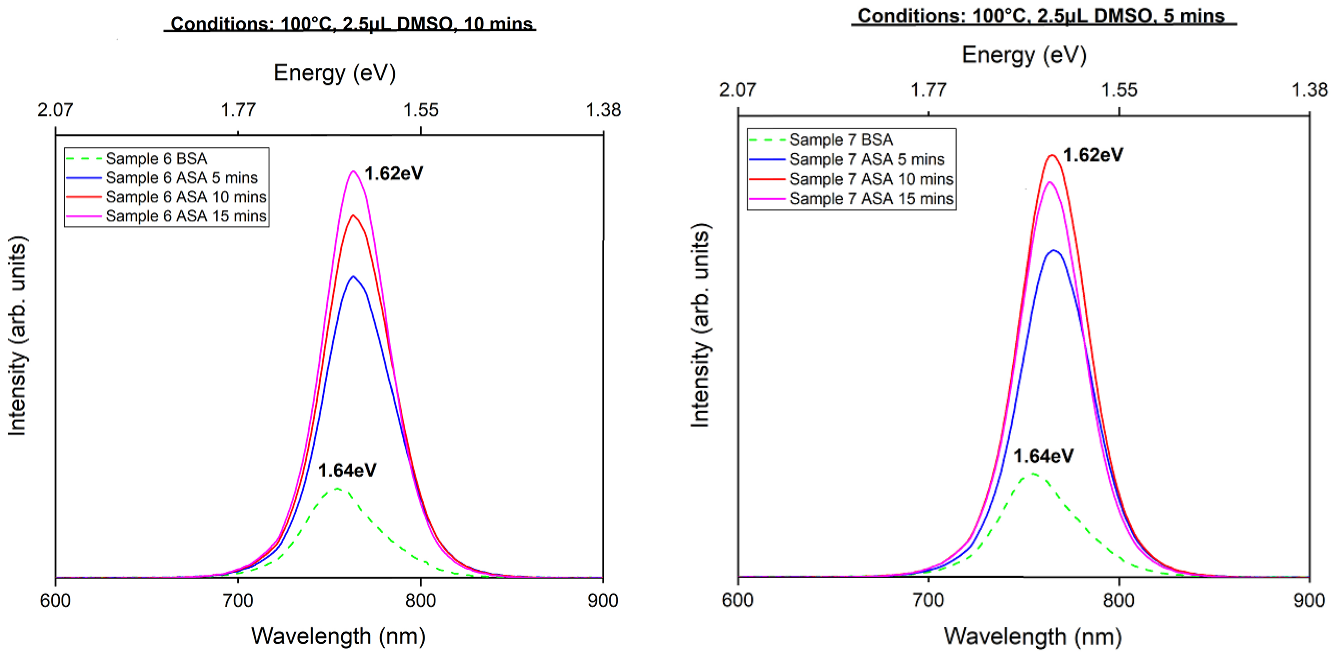

Figure 29: PL result for Sample 6 and 7 BSA and ASA. ASA is measured after 5,10 and 15 minutes.

Name	Band gap (BSA)	Band gap (ASA)	PL peak FWHM (BSA)	PL peak FWHM (ASA)		
				After 5 mins	After 10 mins	After 15 mins
Sample 6	1.64 eV	1.62 eV	46 nm	45.5 nm	44 nm	41 nm
Sample 7	1.64 eV	1.62 eV	46 nm	43.5 nm	42 nm	40.5 nm

Table 4: The calculated BSA/ASA band gaps and PL peak FWHM of the Sample 6 and 7.

Among all the samples tested with different SA conditions and methods, Sample 6 exhibits the most desirable results across XRD, AFM, and PL analyses. Sample 6 underwent the SA treatment at 100°C with 2.5 µL DMSO for 10 mins. In the XRD analysis, it displayed a higher intensity of the perovskite peak compared to the PbI_2 precursor peaks, indicating a higher degree of conversion of the perovskite phase compared to the other samples. The AFM images

of Sample 6 exhibited continuous and measurable $MAPbI_3$ grains, with an increase in grain size from 32.5 to 75 nm. While the grain size increase may be small, it confirms the effectiveness of the SA treatment in promoting grain growth. In terms of PL, Sample 6 demonstrated a trend of increasing PL intensity over the measured time.

On the other hand, Sample 7, subjected to a shorter SA time of 5 mins, does not yield better results than Sample 6. The presence of excess of PbI_2 precursor in Sample 7, potentially indicates that the limited exposure time during the SA process might have restricted the time needed for the desired perovskite formation. Despite this, it still exhibited better results overall compared to the other samples treated under SA method 1.

These findings align with our proposed hypothesis of utilizing shorter SA times and an open-top configuration, as employed in SA method 2, to facilitate the removal of DMSO and thereby allowing the recrystallisation of the perovskite phase, while removing the sample from the hot plate to minimize the risk of thermal degradation. Thus, the results obtained from Sample 6 and 7 further support our proposed hypothesis.

5. CONCLUSIONS

Based on the discussions and analysis presented in this study, several key conclusions can be drawn regarding the solvent annealing treatment and characterization of the epitaxial $MAPbI_3$ thin films.

The SA method 1 did not yield the desired outcomes in terms of grain growth and perovskite formation. The XRD results showed a higher intensity of the PbI_2 precursor peaks and a lower intensity of the perovskite phase peak, indicating a lower conversion to the perovskite phase and the presence of excess PbI_2 precursor on the surface. The AFM images exhibited non-uniform and discontinuous grain structures, further confirming the limitations of this method. However, despite the undesired results, a trend of larger grains was still evident, indicating that the SA treatment does contribute to grain size increase. It is proposed that the ineffectiveness of SA method 1 can be attributed to the prolonged exposure of $MAPbI_3$ under DMSO vapour, leading to thermal degradation and decomposition of the perovskite over time. This decomposition process causes the MAI precursor to escape from the surface of the thin films. To address these limitations, there is a need for faster removal of DMSO and shorter SA times to prevent prolonged exposure and minimize thermal degradation.

In response to these challenges, SA method 2 was introduced as an alternative, optimized approach. SA method 2 involves shorter SA times and an open-top set-up, which allows for the rapid removal of the solvent and mitigates the risk of thermal degradation. The results obtained from the samples treated under SA method 2 demonstrated improvements compared to SA method 1. Sample 6 treated under SA method 2 with the specific conditions of 100°C, 2.5 μL DMSO, and 10 mins exhibited the most significant improvements. These included a reduced presence of the PbI_2 precursor, higher perovskite conversion, larger and continuous grain structures with an increase in grain size from 32.5 to 75 nm, and increased PL intensity over time. Epitaxy however is not maintained.

These findings emphasize the importance of precise control and optimization of SA parameters for achieving desirable results in terms of grain growth, perovskite conversion, and optical properties. SA method 2 emerges as a more effective approach for obtaining desired results in SA treatments. Nonetheless, due to the time constraints of the thesis, further research and experimentation are necessary to optimize the SA treatment for additional grain growth and preservation of epitaxy. Sample 6 serves as a promising starting point for further optimization of the SA parameters and potentially exploring modifications to the SA set-up as well. Longer or shorter times under SA method 2 could be explored as the next step. By gaining a deeper understanding of the SA treatment, it is possible to advance the development of high-quality epitaxial $MAPbI_3$ perovskite thin films, useful for solar cell applications.

6. REFERENCES

[1] Jungbluth, N., Stucki, M., Frischknecht, R., & Buesser, S. (2009). Photovoltaics. Sachbilanzen von Energiesystemen: Grundlagen für den ökologischen Vergleich von Energiesystemen und den Einbezug von Energiesystemen in Ökobilanzen für die Schweiz. ecoinvent report, (6-XII), 16-69. Swiss Centre for Life Cycle Inventories, Dübendorf

[2] Dou, L., You, J., Hong, Z., Xu, Z., Li, G., Street, R.A. and Yang, Y. (2013), 25th Anniversary Article: A Decade of Organic/Polymeric Photovoltaic Research. Adv. Mater., 25: 6642-6671. https://doi.org/10.1002/adma.201302563

[3] Jena, A. K., Kulkarni, A., & Miyasaka, T. (2019). Halide Perovskite Photovoltaics: Background, Status, and Future Prospects. Chemical reviews, 119(5), 3036–3103. https://doi.org/10.1021/acs.chemrev.8b00539

[4] NREL. (2023) Chart of Best Research-Cell Efficiencies Provided by NREL https://www.nrel.gov/pv/cell-efficiency.html

[5] Chouhan, L., Ghimire, S., Subrahmanyam, C., Miyasaka, T., & Biju, V. (2020). Synthesis, optoelectronic properties and applications of halide perovskites. Chemical Society Reviews, 49(10), 2869–2885. https://doi.org/10.1039/c9cs00848a

[6] Nande, A., Raut, S., & Dhoble, S. (2021). Perovskite solar cells. *Energy Materials: Fundamentals to Applications*, p249-281. https://doi.org/10.1016/B978-0-12-823710-6.00002-9, Elsevier, ISBN:978-0-12-823710-6

[7] Saliba, M., Orlandi, S., Matsui, T. et al. (2016). A molecularly engineered hole-transporting material for efficient perovskite solar cells. Nat Energy 1, 15017. https://doi.org/10.1038/nenergy.2015.17

[8] Chen, Z., Turedi, B., Alsalloum, A. Y., Yang et al. (2019). Single-crystal MAPbI3 perovskite solar cells exceeding 21% power conversion efficiency. *ACS Energy Letters*, 4(6), 1258-1259. https://doi.org/10.1021/acsenergylett.9b00847

[9] Wu, Y., Xie, F., Chen, H. et al. (2017). Thermally stable MAPbI3 perovskite solar cells with efficiency of 19.19% and area over 1 cm2 achieved by additive engineering. *Advanced materials*, 29(28), 1701073. https://doi.org/10.1002/adma.201701073

[10] Gao, W., Zhang, Z., Xu, R., Chan, E. M., Yuan, G., & Liu, J. (2022). Development and Prospects of Halide Perovskite Single Crystal Films. *Advanced Electronic Materials*, *8*(4), 2100980. https://doi.org/10.1002/aelm.202100980

[11] Cheng, X., Yang, S., Cao, B., Tao, X., & Chen, Z. (2019). Single Crystal Perovskite Solar Cells: Development and Perspectives. *Advanced Functional Materials*, *30*(4), 1905021. https://doi.org/10.1002/adfm.201905021

[12] Dong, Q., Fang, Y., Shao, Y., Mulligan, P., Qiu, J., Cao, L., & Huang, J. (2015). Electron-hole diffusion lengths > 175 μm in solution-grown CH3NH3PbI3 single crystals. *Science*, 347(6225), pp. 967-970. https://doi.org/10.1126/science.aaa5760

[13] Yu, Y., Wang, C., Grice, C. et al. (2017). Synergistic effects of lead thiocyanate additive and solvent annealing on the performance of wide-bandgap perovskite solar cells. *ACS Energy Letters*, 2(5), 1177-1182. https://doi.org/10.1021/acsenergylett.7b00278

[14] Zhang, F., Zhu, K., (2020) Additive Engineering for Efficient and Stable Perovskite Solar Cells. Adv. Energy Mater. 10, 1902579. https://doi.org/10.1002/aenm.201902579

[15] Pereyra, C., Xie, H., & Lira-Cantu, M. (2021). Additive engineering for stable halide perovskite solar cells. Journal of Energy Chemistry, 60, 599-634. https://doi.org/10.1016/j.jechem.2021.01.037

[16] Zhou, H., Chen, Q., Li, G., Luo, S., Song et al. (2014). Interface engineering of highly efficient perovskite solar cells. Science, 345(6196), 542-546. https://doi.org/10.1126/science.1254050

[17] Yu, W., Sun, X., Xiao, M. et al. (2022). Recent advances on interface engineering of perovskite solar cells. Nano Res. 15, 85–103. https://doi.org/10.1007/s12274-021-3488-7

[18] Jeon, N., Noh, J., Kim, Y. et al. (2014). Solvent engineering for high-performance inorganic–organic hybrid perovskite solar cells. Nature Mater 13, 897–903. https://doi.org/10.1038/nmat4014

[19] Wu, T., Wu, J., Tu, Y., He, X., Lan, Z., Huang, M., & Lin, J. (2017). Solvent engineering for high-quality perovskite solar cell with an efficiency approaching 20%. Journal of Power Sources, 365, 1-6. https://doi.org/10.1016/j.jpowsour.2017.08.074

[20] Huang, F., Dkhissi, Y., Huang, W. et al. (2014). Gas-assisted preparation of lead iodide perovskite films consisting of a monolayer of single crystalline grains for high efficiency planar solar cells. Nano Energy, 10, 10-18. https://doi.org/10.1016/j.nanoen.2014.08.015

[21] Eze, V. O., Lei, B., & Mori, T. (2016). Air-assisted flow and two-step spin-coating for highly efficient CH3NH3PbI3 perovskite solar cells. Japanese Journal of Applied Physics, 55(2S), 02BF08. https://doi.org/10.7567/JJAP.55.02BF08

[22] Cassella, E. J., Spooner, E. L., Thornber, T. et al. (2022). Gas-assisted spray coating of perovskite solar cells incorporating sprayed self-assembled monolayers. Advanced Science, 9(14), 2104848. https://doi.org/10.1002/advs.202104848

[23] Eze, V. O., & Mori, T. (2016). Enhanced photovoltaic performance of planar perovskite solar cells fabricated in ambient air by solvent annealing treatment method. Japanese Journal of Applied Physics, 55(12), 122301. https://doi.org/10.7567/JJAP.55.122301

[24] Xiao, Z., Dong, Q., Bi, C., Shao, Y., Yuan, Y., & Huang, J. (2014). Solvent annealing of perovskite-induced crystal growth for photovoltaic-device efficiency enhancement. Advanced Materials, 26(37), 6503-6509. https://doi.org/10.1002/adma.201401685

[25] Liu, J., Gao, C., He, X. et al.. (2015). Improved crystallization of perovskite films by optimized solvent annealing for high efficiency solar cell. ACS applied materials & interfaces, 7(43), 24008-24015. https://doi.org/10.1021/acsami.5b06780

[26] Game, O. S., Smith, J. A., Alanazi, T. I. (2020). Solvent vapour annealing of methylammonium lead halide perovskite: what's the catch?. Journal of Materials Chemistry A, 8(21), 10943-10956. https://doi.org/10.1039/D0TA03023F

[27] Omer, M.I., Xizu, W., Xiaohong, T. (2022). Solvent Vapor Annealing of Perovskite Films for High Performance Perovskite Solar Cells: A Mini-Review. Polymer Sci peer Rev J. 3(3). PSPRJ. 000563. 2022. https://doi.org/10.31031/PSPRJ.2022.03.000563

[28] IMS | Inorganic Materials Science (n.d). *University of Twente*. https://www.utwente.nl/en/tnw/ims/

[29] Zhou, Z., Qiao, H. W., Hou, Y., Yang, H. G., & Yang, S. (2021). Epitaxial halide perovskite-based materials for photoelectric energy conversion. *Energy & Environmental Science*, 14(1), 127-157. https://doi.org/10.1039/D0EE02902E

[30] Fang, Z, Yan, N, Liu, S(F). (2022). Modulating preferred crystal orientation for efficient and stable perovskite solar cells—From progress to perspectives. InfoMat. 4(10):e12369. https://doi.org/10.1002/inf2.12369

[31] Dunlap-Shohl, W. A., Zhou, Y., Padture, N. P., & Mitzi, D. B. (2019). Synthetic Approaches for Halide Perovskite Thin Films. Chemical reviews, 119(5), 3193–3295. Chapter 1. https://doi.org/10.1021/acs.chemrev.8b00318

[32] Ong, K. P., Goh, T. W., Xu, Q., & Huan, A. (2015). Structural Evolution in Methylammonium Lead Iodide CH3NH3PbI3. The journal of physical chemistry. A, 119(44), 11033–11038. https://doi.org/10.1021/acs.jpca.5b09884

[33] Whitfield, P., Herron, N., Guise, W. et al. (2016). Structures, Phase Transitions and Tricritical Behavior of the Hybrid Perovskite Methyl Ammonium Lead Iodide. Sci Rep 6, 35685 (2016). https://doi.org/10.1038/srep35685

[34] M. Safdari, A. Fischer, B. Xu, L. Kloo and J. M. Gardner. (2014). Structure and function relationships in alkylammonium lead(II) iodide solar cells, J. Mater. Chem. A, 2015, 3, 9201–9207. https://doi.org/10.1039/C4TA06174H

[35] Peng H, Su Z, Zheng Z, Lan H, Luo J, Fan P, Liang G. (2019). High-Quality Perovskite $CH_3NH_3PbI_3$ Thin Films for Solar Cells Prepared by Single-Source Thermal Evaporation Combined with Solvent Treatment. Materials (Basel). 15;12(8):1237. https://doi.org/10.3390/ma12081237, PMID: 30991739; PMCID: PMC6514769.

[36] Rothmann, M. U., Li, W., Etheridge, J., Cheng, Y.-B., (2017) "Microstructural Characterisations of Perovskite Solar Cells – From Grains to Interfaces: Techniques, Features, and Challenges" Adv. Energy Mater. 2017, 7, 1700912. https://doi.org/10.1002/aenm.201700912

[37] Dunlap-Shohl, W. A., Zhou, Y., Padture, N. P., & Mitzi, D. B. (2019). Synthetic Approaches for Halide Perovskite Thin Films. Chemical reviews, 119(5), 3193–3295. Chapter 3. https://doi.org/10.1021/acs.chemrev.8b00318

[38] Bachmann, K. (2001). Epitaxy. Encyclopedia of Materials: Science and Technology (Second Edition), 2791-2799. https://doi.org/10.1016/B0-08-043152-6/00496-4

[39] Keuch T.F. (2014). Handbook of crystal growth Second Edition: Thin films and epitaxy. Elsevier, Chapter 1. ISBN: 978-0444633040

[40] Krebs, H.U., Weisheit, M., Faupel, J., et al. (2003). Pulsed Laser Deposition (PLD) -- A Versatile Thin Film Technique. In: Kramer, B. (eds) Advances in Solid State Physics. Advances in Solid State Physics, vol 43. Springer, Berlin, Heidelberg. https://doi.org/10.1007/978-3-540-44838-9_36

[41] Manser, J.S., Christians, J.A., and Kamat, P.V. (2016). Intriguing Optoelectronic Properties of Metal Halide Perovskites. Chemical Reviews 116 (21), 12956-13008 https://doi.org/10.1021/acs.chemrev.6b00136

[42] Zhong, M., Zeng, W., Tang, H., Wang, L., Liu, F., Tang, B., & Liu, Q. (2019). Band structures, effective masses and exciton binding energies of perovskite polymorphs of CH3NH3PbI3. Solar Energy, 190, 617-621. https://doi.org/10.1016/j.solener.2019.08.055

[43] Chen, Y., He, M., Peng, J., Sun, Y., Liang, Z. (2016). Structure and Growth Control of Organic–Inorganic Halide Perovskites for Optoelectronics: From Polycrystalline Films to Single Crystals. Adv. Sci., 3: 1500392. https://doi.org/10.1002/advs.201500392

[44] Qian, K., Yu, L., Jingnan S. et al. (2021). Understanding the synergistic effect of mixed solvent annealing on perovskite film formation. Chinese Physics B. Vol30. No.6. https://doi.org/10.1088/1674-1056/abdb1f

[45] Liuwen, T., Zhang, W., Yu, H. et al. (2019). Post-treatment of Perovskite Films toward Efficient Solar Cells via Mixed Solvent Annealing. ACS Applied Energy Materials. 2. 4954-4963. https://doi.org/10.1021/acsaem.9b00613

[46] Yi, A., Chae, S. et al. (2019). Synergistic effect of cooperating solvent vapor annealing for high-efficiency planar inverted perovskite solar cells. Journal of Materials Chemistry A. 7. https://doi.org/10.1039/C9TA08791E

[47] Ta,n W.L. and McNeill, C.R. (2022). X-ray diffraction of photovoltaic perovskites: Principles and applications. Applied Physics Reviews; 9 (2): 021310. https://doi.org/10.1063/5.0076665

[48] König, U., Angélica R., Norberg, N. et al. (2012). Rapid X-ray diffraction (XRD) for grade control of bauxites. Conference: ICSOBA.

[49a] Voigtländer, B. (2019). Atomic Force Microscopy. NanoScience and Technology. Springer, Cham. Chapter 1, pp. 1-13. https://doi.org/10.1007/978-3-030-13654-3

[49b] Voigtländer, B. (2019). Atomic Force Microscopy. NanoScience and Technology. Springer, Cham. Chapter 14, pp. 231-253. https://doi.org/10.1007/978-3-030-13654-3

[50] Gilliland, G. (1997). Photoluminescence spectroscopy of crystalline semiconductors. Materials Science and Engineering: R: Reports, 18(3-6), 99-399. https://doi.org/10.1016/S0927-796X(97)80003-4

[51] Mahalingam, V. (2018). Synthesis, growth and characterization of piperazinium p-aminobenzoate and piperazinium p-chlorobenzoate nonlinear optical single crystals. https://doi.org/10.13140/RG.2.2.16046.82243

[52] Lopes, J.M.S., Barbosa Neto, N.M., Araujo, P.T. (2022). An Introduction to Steady-State and Time-Resolved Photoluminescence. pp.131-144 In: Bahnemann, D., Patrocinio, A.O.T. (eds) Springer Handbook of Inorganic Photochemistry. Springer Handbooks. Springer, Cham. https://doi.org/10.1007/978-3-030-63713-2_6

[53] Kumar, S., Houben, L., Katya Rechav, & Cahen, D. (2022). Halide perovskite dynamics at work: Large cations at 2D-on-3D interfaces are mobile. PNAS 119(10). https://doi.org/10.1073/pnas.2114740119

[54] Quarti, C., Mosconi, E., Ball, J. et al. (2015). Structural and optical properties of methylammonium lead iodide across the tetragonal to cubic phase transition: Implications for perovskite solar cells. Energy and Environmental Science 9(1):155-163. https://doi.org/10.1039/C5EE02925B

[55] Kim, NK., Min, Y.H., Noh, S. et al. (2017). Investigation of Thermally Induced Degradation in CH3NH3PbI3 Perovskite Solar Cells using In-situ Synchrotron Radiation Analysis. Sci Rep 7, 4645. https://doi.org/10.1038/s41598-017-04690-w

7. APPENDICES

A. Supplementary AFM images

The samples to which each AFM images belong are depicted on top of the image. Some images are more distorted from the other because of the AFM drift or the AFM tip picking up molecules, thus they can be treated as artifacts.

[1x1] AFM images

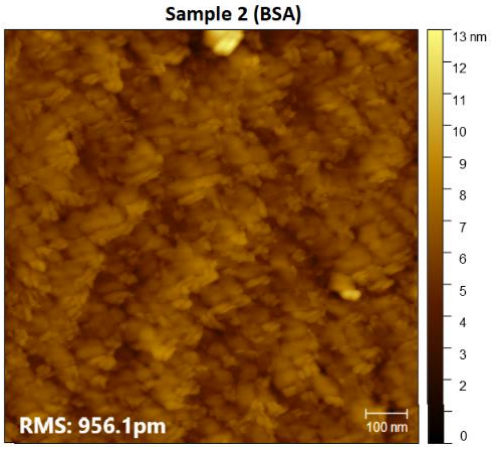

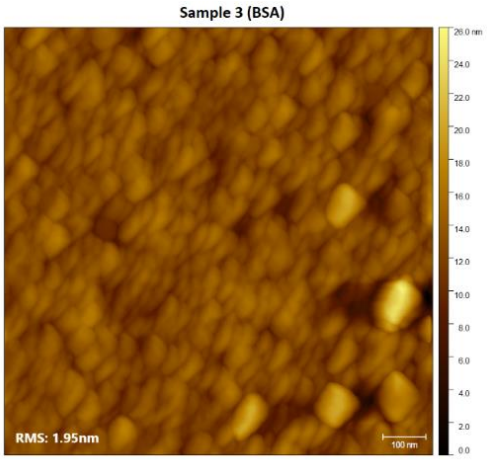

[5x5] AFM images

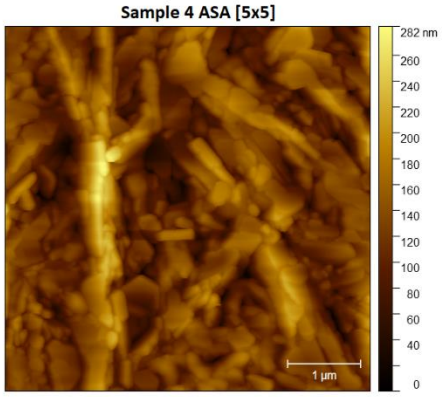

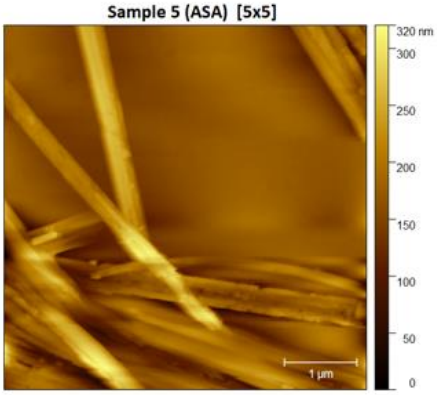

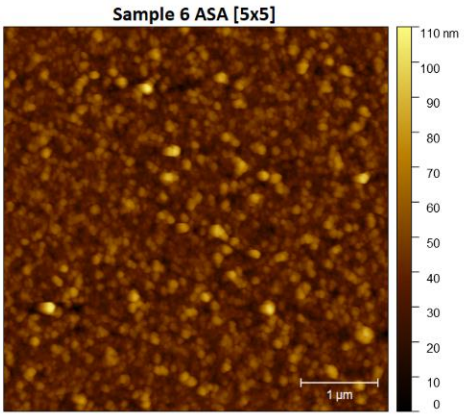

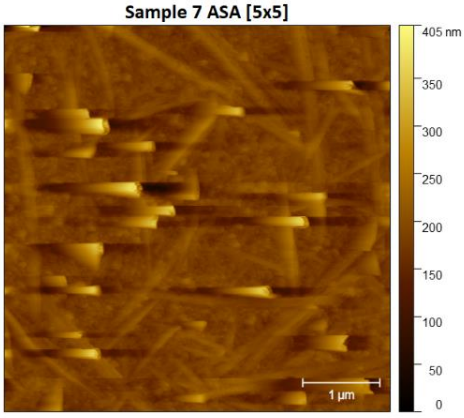

B. Colour change of all samples after solvent annealing

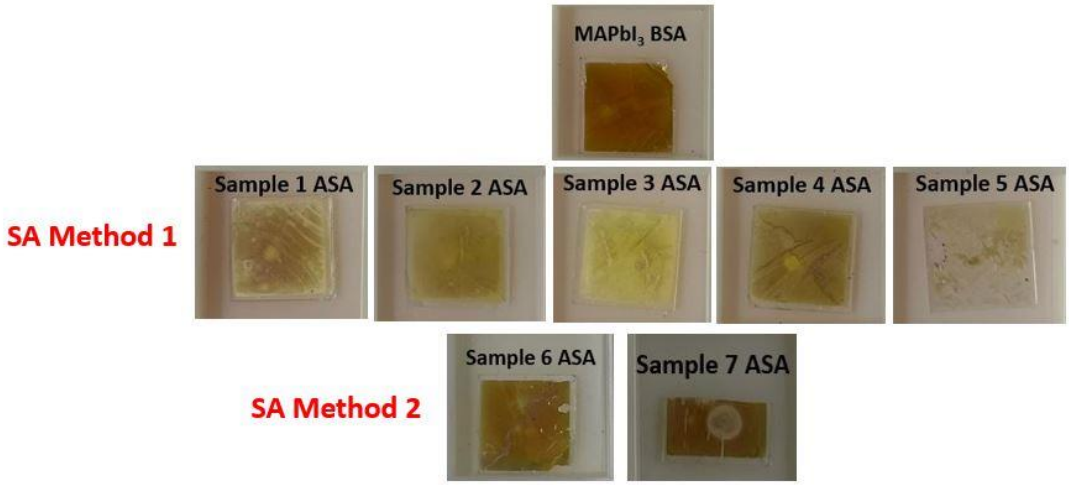

C. Normalized PL intensity results

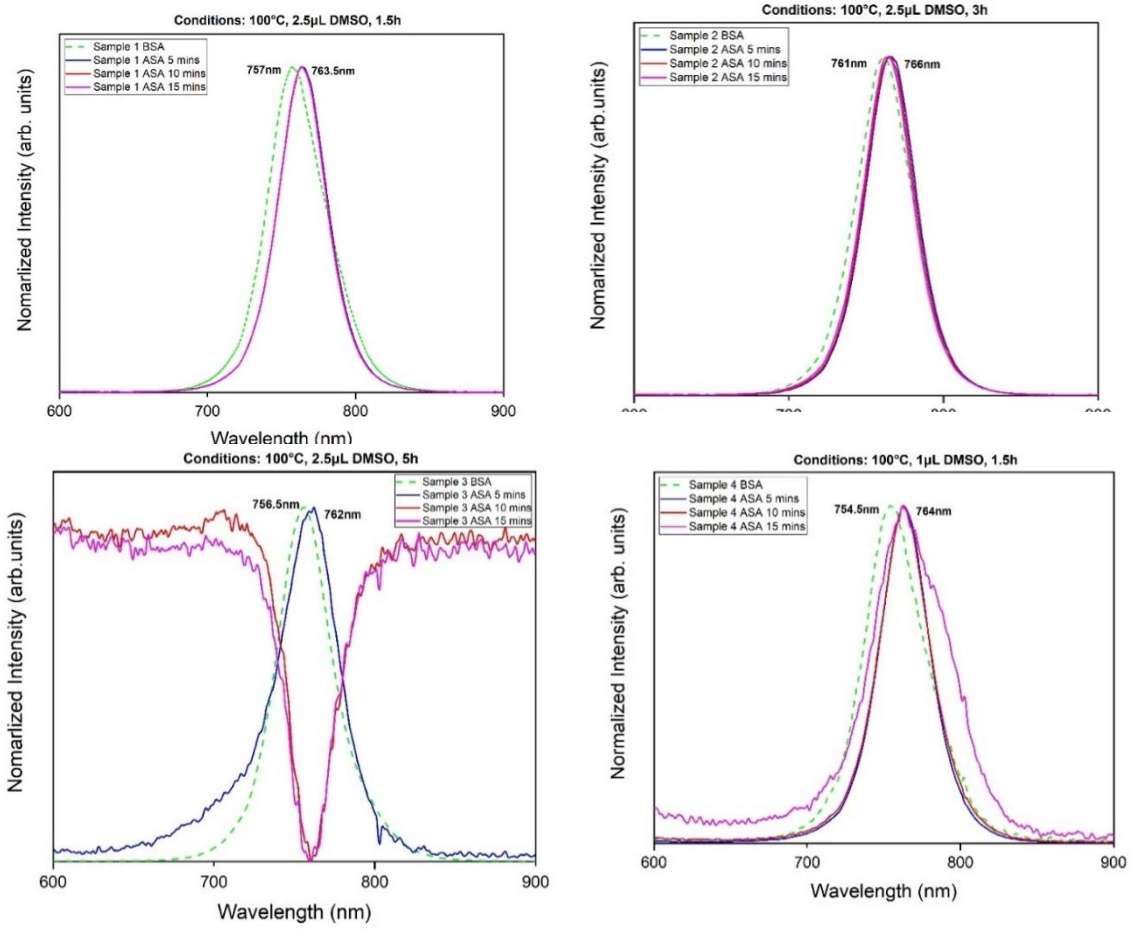

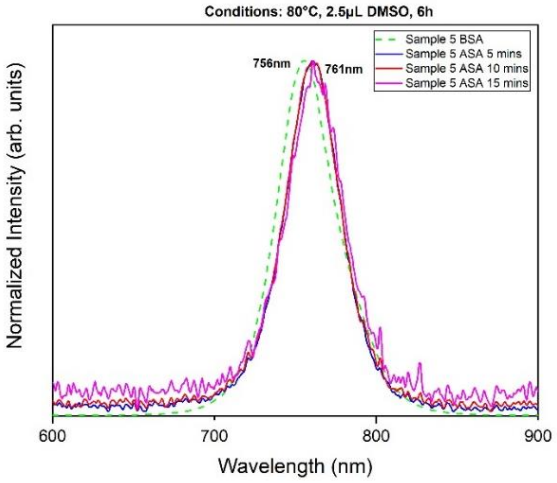
Conditions: 80°C, 2.5µL DMSO, 6h
Sample 5 BSA
Sample 5 ASA 5 mins
Sample 5 ASA 10 mins
Sample 5 ASA 15 mins
756nm
761nm
Normalized Intensity (arb. units)
600
700
800
900
Wavelength (nm)

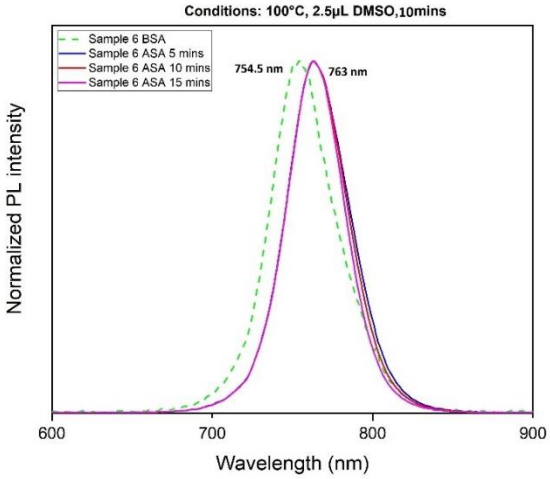
Conditions: 100°C, 2.5µL DMSO,10mins
Sample 6 BSA
Sample 6 ASA 5 mins
Sample 6 ASA 10 mins
Sample 6 ASA 15 mins
754.5 nm
763 nm
Normalized PL intensity
600
700
800
900
Wavelength (nm)

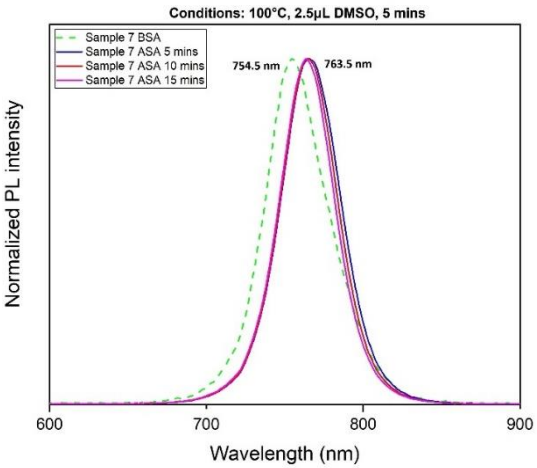
Conditions: 100°C, 2.5µL DMSO, 5 mins
Sample 7 BSA
Sample 7 ASA 5 mins
Sample 7 ASA 10 mins
Sample 7 ASA 15 mins
754.5 nm
763.5 nm
Normalized PL intensity
600
700
800
900
Wavelength (nm)